

1

2

3

4

5

6

7

**Radium isotopes to trace uranium redox anomalies in anoxic groundwater**

8

Lindsay Krall, Luis Auqué-Sanz, Jordi Garcia-Orellana, Giada Trezzi, Eva-Lena Tullborg,  
Juhani Suksi, Don Porcelli, Per Andersson

9

10

11

## Abstract

$^{223}\text{Ra}$ ,  $^{224}\text{Ra}$ ,  $^{226}\text{Ra}$ , and  $^{228}\text{Ra}$  isotopes have been measured in groundwaters from depths ranging 50 – 900 m in fractured crystalline bedrock (Forsmark, Sweden) to understand the reason for elevated (up to 150  $\mu\text{g/L}$ ) aqueous uranium ( $\text{U}_{\text{aq}}$ ) at 400-650 m depth. Ra isotope data is interpreted alongside previously reported  $^{222}\text{Rn}$ ,  $^{234}\text{U}$ , and  $^{238}\text{U}$  data, as well as PHREEQC geochemical modelling and uranium mineralogy. A novel,  $[\text{}^{223}\text{Ra}/\text{}^{226}\text{Ra}]_{\text{GW}}$ -based approach (where brackets and “GW” subscript refer to expression of an activity ratio measured from groundwater) to groundwater residence time estimation shows that elevated  $[\text{U}_{\text{aq}}]$  is most common in Holocene-age groundwaters of marine origin. Although these groundwaters are geochemically reducing, the  $[\text{}^{223}\text{Ra}/\text{}^{228}\text{Ra}]_{\text{corr}}$  (where “corr” subscript refers to a correction applied to compare  $[\text{}^{223}\text{Ra}/\text{}^{228}\text{Ra}]_{\text{GW}}$  to the more commonly reported  $[\text{}^{226}\text{Ra}/\text{}^{228}\text{Ra}]_{\text{GW}}$ ) suggest that they interact with U-rich pegmatites containing Proterozoic- and Palaeozoic-age Ca-U(VI)-silicate minerals, which are undersaturated in the present groundwaters. Local aqueous U(VI) can be stabilized in  $\text{Ca}_2\text{UO}_2\text{CO}_3^0$  complexes at pe-values as low as  $-4.5$  but is susceptible to reduction after a modest decrease in pe-value, alkalinity, or Ca concentration. The  $[\text{}^{223}\text{Ra}/\text{}^{228}\text{Ra}]_{\text{corr}}$  and  $[\text{}^{224}\text{Ra}/\text{}^{228}\text{Ra}]_{\text{GW}}$  also suggest that  $\text{U(VI)}_{\text{aq}}$  precipitates as  $\text{UO}_{2+\text{X}}$  at the interface between marine and non-marine groundwaters. From these data, local  $[\text{U}_{\text{aq}}]$  is proposed to be governed by on-going water-rock interaction involving old U(VI)-minerals.

## 1    **1    Introduction**

2    To immobilize spent nuclear fuel, a geologic repository must be sited in a chemically reducing  
 3    environment, wherein the insoluble U(IV) state dominates the speciation of uranium. Redox potentials  
 4    and dissolved uranium ( $U_{aq}$ ) concentrations are usually low at depth in crystalline rocks (Gascoyne, 2004;  
 5    Gimeno et al., 2006 and references therein). However, in fractured meta-granite at Forsmark, Sweden,  
 6    which hosts a low-level waste repository (SFR) and may eventually host a spent fuel repository, elevated  
 7     $U_{aq}$  (20 – 150  $\mu\text{g U/L}$ ) is present in low redox groundwaters at repository depth (~500 m.). The Swedish  
 8    Nuclear Fuel and Waste Management Company (SKB) is investigating whether this  $U_{aq}$  was oxidized and  
 9    maintained by the glacial and marine groundwaters introduced during the Holocene. Since similar events  
 10    will recur within the time-frame of repository safety, the effects of deglaciation on the deep redox system  
 11    must be understood.

12    At Forsmark,  $[U_{aq}]$  can be, but is not invariably, high in the bicarbonate-rich Holocene groundwaters of  
 13    marine origin, particularly those recovered from the bedrock zones showing brittle deformation. From  
 14    these relations, Smellie et al. (2008) inferred that  $U_{aq}$  is sourced by minerals in the Forsmark fractures and  
 15    maintained by aqueous U(VI)-carbonate complexes. Indeed, the aqueous  $\text{Ca}_2\text{UO}_2(\text{CO}_3)_3^0$  complex, which  
 16    inhibits  $\text{U(VI)}_{aq}$  reduction (e.g. Fox et al., 2006; Singer et al., 2009, Stewart et al., 2011), was found at  
 17    depths exceeding 500 m (Tullborg et al., 2017). Furthermore, Ca-U(VI)-silicate minerals preserve  
 18    evidence of partial oxidation of U(IV), originally deposited in uraninite and uranothorite minerals, during  
 19    the geologically early events of hydrothermal fluid circulation that affected the Forsmark bedrock (Krall  
 20    et al., 2015, 2019). Rather than U(VI)-minerals of Holocene origin, the Precambrian & Palaeozoic Ca-  
 21    U(VI)-silicates may be an important source of  $U_{aq}$  to the bicarbonate-rich marine groundwaters. Here, we  
 22    explore these two hypotheses using short-lived U- and Th-series nuclides and geochemical modelling.

23    Natural waters contain four Ra isotopes:  $^{228}\text{Ra}$  ( $t_{1/2}$  5.75 y) and  $^{224}\text{Ra}$  ( $t_{1/2}$  3.63 d) of the  $^{232}\text{Th}$ -series, and  
 24     $^{223}\text{Ra}$  ( $t_{1/2}$  11.4 d) and  $^{226}\text{Ra}$  ( $t_{1/2}$  1600 y) of the  $^{235}\text{U}$ - and  $^{238}\text{U}$ -series, respectively (Krishnaswami &  
 25    Cochran, 2008; Figure 1). Following decay of Th parents, aquifer solids supply Ra to the groundwater  
 26    ( $\text{Ra}_{GW}$ ) through dissolution, desorption, and alpha recoil, i.e. the physical ejection of a recoil nucleus  
 27    following alpha decay of its parent (Kigoshi, 1971; Fleischer & Raabe, 1978; Figure 1). If  $\text{Ra}_{GW}$  activities  
 28    are in steady state, where their supply and removal fluxes are balanced,  $\text{Ra}_{GW}$  activity ratios (ARs) reflect  
 29    the relative importance of the processes to water-rock interaction (Porcelli & Swarzenski, 2003; Porcelli,  
 30    2008). Since decay constants govern the evolution to steady state, short-lived  $^{223}\text{Ra}_{GW}$  activities arrive at  
 31    steady state before  $^{226}\text{Ra}_{GW}$ , so  $[^{223}\text{Ra}/^{226}\text{Ra}]_{GW}$  (brackets denote an AR) can be used to estimate residence  
 32    times for Holocene-age groundwaters (Davidson & Dickson, 1986; Porcelli, 2008). The  $\text{Ra}_{GW}$  also

reflects the abundance of parent isotopes in the aquifer solids, so ARs of U- to Th-series  $Ra_{GW}$  (e.g.  $[^{226}Ra/^{228}Ra]_{GW}$ ) can be used to determine the U/Th ratio of the host rock ( $[^{238}U/^{232}Th]_{solid}$ ).

To complement the description of the early evolution of the Forsmark redox system (Krall et al., 2015, 2019), the Holocene water-rock interactions are here probed using Ra isotopes. Groundwater residence time and  $[^{238}U/^{232}Th]_{solid}$  were determined because they have implications for reaction kinetics and solid-phase sources of uranium ( $U_{solid}$ ). Interpretation of the  $Ra_{GW}$  will be supplemented by PHREEQC geochemical modelling in order to clarify the response of the deep redox system to surface water incursions following deglaciation and sea-level rise.

## 2 Study site

Along the Baltic Sea coast 120 km north of Stockholm, Sweden, Forsmark and SFR have been assessed as discrete sites despite their proximity (Figure 2.a) because they (will) accept distinct waste streams: spent fuel and short-lived, low-level radioactive waste, respectively. The Forsmark bedrock is dominated by calc-alkaline, meta-granite with scattered pegmatites and SFR by pegmatitic rock (1.9 – 1.8 Ga; Stephens et al. 2005; Hermansson et al., 2007; Hermansson et al., 2008). Bedrock fractures formed during several Precambrian and Palaeozoic events of brittle deformation (Figure 2). During these events, hydrothermal fluids circulated and precipitated the minerals that presently coat the hydraulically conductive fractures (e.g. hematite, chlorite, calcite, and pyrite; Sandström et al. 2009).

### 2.1 Groundwater origin and mixing

The present groundwater chemistry has been produced in response to (de)glaciation and changing sea levels, and water-rock interactions over time (Laaksoharju et al., 2008). Fresh meteoric water and brackish Littorina Sea water (a 9000-5000 BP stage of the Baltic Sea) dominate the uppermost 20 – 200 m. A mixture of Littorina Sea water, older glacial melt water, and old saline basement water (>1.5 Ma; Smellie et al., 2008) extends from 200 to 300 or 700 m depth, depending on zonal fracture frequency (“brackish-marine”). The deepest groundwaters are a mixture between glacial meltwater and saline basement water (“non-marine”; Laaksoharju et al., 2008). A transitional layer with a minor Littorina component lies between the brackish marine and brackish-to-saline non-marine groundwaters (“transition”; Figure 2.b). At SFR (50 – 400 m.b.s.l), the same end-members are found together with modern Baltic Sea water (Figure 2.c; “mixed”), which was introduced after construction of the subsea repository (Nilsson et al., 2011).

Forsmark groundwaters at depths greater than 300 m represent a disconnected fracture network rather than one with well-defined flow lines (Laaksoharju et al., 2008). SFR groundwaters reflect a more

connected system with strong mixing in the subhorizontal fracture zone, though some vertical fractures have isolated dilute glacial meltwater (“glacial”; Nilsson et al., 2011).

## 2.2 *Dissolved uranium*

At Forsmark,  $[U_{aq}]$  is highest (up to 150  $\mu\text{g/L}$ ) in the brackish-marine groundwaters (compare to 3  $\mu\text{g/L}$  in seawater) at 400 – 600 m depth with redox potentials (Eh) of –140 to –200 mV relative to Pt, Au, and C electrodes (Auqué et al., 2008; Laaksoharju et al., 2008). The  $[U_{aq}]$  and redox potentials are lower in groundwaters deeper than 600 m and in bedrock domains with low brittle deformation. Mixed groundwaters with  $10 \mu\text{g/L} > [U_{aq}] < 60 \mu\text{g/L}$  dominate the SFR site ( $Eh \geq -190$  mV). Here, elevated  $[U_{aq}]$  is related to alkalinity  $> 50 \text{ mg HCO}_3^-/\text{L}$  (Nilsson et al., 2011). Previous speciation-solubility calculations indicated that aqueous U(VI)-carbonate complexes can persist where U(VI) sources interact with low-redox groundwaters that have  $\text{HCO}_3^- > 30 \text{ mg/L}$ . Since  $U_{aq}$  is not unequivocally associated with a specific groundwater type, Smellie et al. (2008) inferred that soluble  $U(VI)_{solid}$  sources are scattered throughout the Forsmark and SFR fracture networks.

Typically, deep groundwaters in crystalline bedrock ( $> 200$  m depth) that have redox potentials and alkalinities similar to Forsmark and SFR show lower  $[U_{aq}]$ , for example at: Laxemar, Sweden ( $< 1 \mu\text{g/L}$ ), Stripa, Sweden ( $< 35 \mu\text{g/L}$ ), Olkiluoto, Finland ( $< 18 \mu\text{g/L}$ ), Palmutto, Finland ( $1 - 10 \mu\text{g/L}$ ; Gimeno et al., 2008 and references therein; Gimeno et al., 2006 and references therein). Nevertheless, high  $[U_{aq}]$  is found elsewhere. For instance, U(VI)-carbonate complexes maintain 300  $\mu\text{g } U_{aq}/\text{L}$  at Lac du Bonnet, Canada (200 – 400 m depth; Gascoyne, 2004).

## 2.3 *Solid-phase uranium*

The crystalline and amorphous  $U_{solid}$  at Forsmark/SFR formed after uraninite and metamict uranothorite in pegmatites were altered by hydrothermal fluids during the region’s early tectonothermal evolution (Sandström et al., 2011; Krall et al., 2015). The oxidized  $U_{solid}$  is persevered as Ca-U(VI)-silicate minerals (haiweeite and uranophane), dated to ~1250 and ~300 Ma (Krall et al., 2019). Recent alteration of these Ca-U(VI)-silicates by carbonate-rich fluids is also evident ( $< 100$  Ma). Finally, a fine-grained, mixed U(IV)/U(VI)-oxide (hereafter “ $UO_{2+x}$ ”) is associated with Fe-Al-silicate fracture minerals (Palaeozoic or younger). The brittle deformation zones surrounding the repository target volume, expressed as open or closed fractures, were preferentially altered by the hydrothermal fluids (Figure 2). During the Quarternary, the  $U_{solid}$  in fractures deeper than 300 m was redistributed, but uranium-series analyses of bulk fracture coatings from Forsmark could not attribute this to a specific event (Smellie et al., 2008).

### 3 Sample description and methods

Groundwaters were sampled from SKB's deep boreholes, which are equipped with a series of packers to prevent mixing during pumping. The sampled KFM and KFR borehole sections (denoting Forsmark and SFR samples, respectively) are shown with respect to depth and local groundwater type in Figure 2.b-c. Borehole sections KFM08A.2(550) and KFM01D.2(340) (where ".X" and "(XYZ)" suffixes refer to the depth of a groundwater section) collect groundwater from a tectonic lens that was affected by only minor brittle deformation and so has a low hydraulic conductivity. Boreholes KFM02B, KFM02A, and KFM03A sample major deformation zones with higher hydraulic conductivities. Groundwater classifications (Section 2.1) are provided in Table 1.

#### 3.1 $^{223}\text{Ra}$ , $^{224}\text{Ra}$ , $^{226}\text{Ra}$ , and $^{228}\text{Ra}$

From each borehole section, two liters of groundwater were passed through columns loaded with 25 g of manganese-impregnated acrylic fiber ("Mn-fiber") to extract the Ra isotopes (Moore 1973; Moore et al. 1995). Since geochemically reducing waters can dissolve the Mn-fiber, two groundwater samples were each filtered through a series of two columns to check the Ra removal yield. These results, together with previous  $^{226}\text{Ra}_{\text{GW}}$  measurements obtained from the SKB Sicada database, did not indicate loss of Ra from the filters (Section 3.2, 4.3.1; Table 2).  $^{223}\text{Ra}$ ,  $^{224}\text{Ra}$ ,  $^{226}\text{Ra}$ , and  $^{228}\text{Ra}$  activities were measured at the Autonomous University of Barcelona.  $^{223}\text{Ra}$  and  $^{224}\text{Ra}$  were measured within seven and three days of collection, respectively, using a Radium Delayed Coincidence Counter (RaDeCC) as described by Moore and Arnold (1996). The  $^{226}\text{Ra}$  and  $^{228}\text{Ra}$  activities were measured using a well-type germanium gamma detector using the  $^{214}\text{Pb}$  and  $^{228}\text{Ac}$  photopeaks at 352 and 911 keV, respectively. Details of sample preparation and analytical corrections can be found in Sun & Torgersen (1998), Charette et al. (2001), and Rodellas et al. (2015). Relative analytical uncertainties for  $^{223}\text{Ra}$ ,  $^{224}\text{Ra}$ ,  $^{226}\text{Ra}$ , and  $^{228}\text{Ra}$  were 9%, 6%, 5%, and 10% (to  $1\sigma$ ), respectively, and were calculated according to Garcia-Solsona et al. (2008).

#### 3.2 $^{222}\text{Rn}$ , $^{234}\text{U}$ and $^{238}\text{U}$ isotopes

$^{234}\text{U}$  and  $^{238}\text{U}$  isotopes are routinely analyzed within the SKB groundwater chemistry monitoring program, and these results were retrieved from the SKB Sicada database.  $^{234}\text{U}$  and  $^{238}\text{U}$  isotopes were analyzed using an Ametec surface barrier alpha spectroscopy system at the Scottish Universities Research and Reactor Centre (e.g. Drake et al., 2009; Mackenzie et al., 1992).  $^{222}\text{Rn}$  and  $^{226}\text{Ra}$  activities, measured between 2002 and 2008, were available for most borehole sections. A RAD7 radon detector was used to measure  $^{222}\text{Rn}$  in the field and Liquid Scintillation Counting was used to measure  $^{226}\text{Ra}$  at the Scottish Universities Environmental Research Center (Grolander, 2009). Analytical uncertainties, due to counting statistics, for each  $^{234}\text{U}$ ,  $^{238}\text{U}$ ,  $^{222}\text{Rn}$  and  $^{226}\text{Ra}$  were  $\leq 5\%$ .

### 3.3 Geochemical data and PHREEQC modelling

Chemical data for the modelling was compiled from the Sicada database (Table 1). Sandström et al. (2011) report the sample preparation, analytical methodology and uncertainties for these data. Measurement precision, reported to  $2\sigma$ , ranged between 4% ( $\text{HCO}_3^-$ ) to 15% (Ba) but were usually ~12%.

Geochemical modelling was performed using the PHREEQC computer program (Parkhurst & Appelo, 2013) together with the Nagra thermodynamic database, which contains stability constants for aqueous  $\text{CaUO}_2(\text{CO}_3)_3^{-2}$  and  $\text{Ca}_2\text{UO}_2(\text{CO}_3)_3^0$  (Thoenen et al., 2014). The thermodynamic data needed to calculate saturation indices of the uranium minerals described by Krall et al. (2015) was primarily compiled from the Thermochemie database (Giffaut et al., 2014), although the solubility constant for haiweeite was obtained from Hemingway (1982). To ensure that uranophane saturation index results were not sensitive to the range of solubility constants reported in the literature, additional thermodynamic data, compiled from Shvareva et al. (2011), Prikryl (2008), and the Wate4f database distributed with PHREEQC, was also provided to the PHREEQC input file.

Speciation-solubility calculations and forward modelling were used to determine the theoretical complexation of aqueous uranium throughout the groundwaters, which has implications on the stability of dissolved U(VI) and U(IV) aqueous species ( $\text{U(VI)}_{\text{aq}}$  and  $\text{U(IV)}_{\text{aq}}$ ). Sensitivity analyses were to determine the effects of minor variations in redox potential or alkalinity on the stability of  $\text{U(VI)}_{\text{aq}}$ . Finally, the  $\text{U}_{\text{aq}}$  sources and sinks for the present groundwaters were assessed by comparing these results to the mineralogical studies by Krall et al. (2015, 2019).

Analytical U(IV), U(VI), and Eh data from the sampled groundwaters were scarce, so the  $\text{U}_{\text{aq}}$  speciation-solubility calculations relied on pe-values calculated from the  $\text{Fe(OH)}_{3(\text{s})}/\text{Fe(II)}$  and the  $\text{S(-II)}/\text{SO}_4^{-2}$  redox couples. These redox species were measured in the field laboratory at Forsmark. Sulfide was analyzed using the methylene blue method using the Swedish ISO standard and Winkler bottles, followed by the procedure outlined in Kamysny et al. (2008). The analytical uncertainty for  $\text{HS}^-$  is as high as 25%. Fe(II) concentrations were determined from filtered (0.45  $\mu\text{m}$ ) and diluted groundwater, using the ferrozine reagent of Stookey (1970) and a spectrophotometer (UVPC2401) at a wavelength of 562 nm. The analytical uncertainty for Fe(II) was 7 to 9%. Calculated pe-values throughout the groundwaters fell within a redox range similar to that indicated by downhole, *in situ* Eh measurements (Gimeno et al., 2008).

The most recent geochemical datasets that co-reported  $^{222}\text{Rn}$  were preferred for the modelling. If the dataset was incomplete or contained an anomalous datum, the most appropriate data(set) was used. For

instance, Fe or HS<sup>-</sup> was absent from a few datasets that reported <sup>222</sup>Rn, so a representative Fe or HS<sup>-</sup> analysis was taken from the monitoring data of the same borehole section for the calculation.

## 4 Results

### 4.1 Geochemistry

The calculated the proportions of U(VI)<sub>aq</sub> and U(IV)<sub>aq</sub> reflect the degree of thermodynamic equilibrium in the U<sub>aq</sub> redox system. Except in brine (e.g. Giblin & Appleyard, 1987), U(IV) is insoluble relative to U(VI), so that in brackish-to-saline groundwater with [U<sub>aq</sub>] > 1 µg/L, such as those occurring at Forsmark/SFR, U(IV) predominance should promote U(IV) precipitation. In the sampled groundwaters, U(VI)<sub>aq</sub> and U(IV)<sub>aq</sub> proportions were sensitive to the redox pair specified for the pe-value calculations, which in turn depended on temperature, pH, and dissolved Fe(II) or S(-II) concentrations. For all groundwater samples, Ca<sub>2</sub>UO<sub>2</sub>(CO<sub>3</sub>)<sub>3</sub><sup>0</sup> dominated the speciation of U(VI)<sub>aq</sub>. For groundwaters in thermodynamic equilibrium with the Fe(II)/Fe(III) redox couple, the U(IV)<sub>aq</sub> predominated the speciation (Figure 3.a). However, equilibrium with the higher pe-values calculated from the S(-II)/S(VI) couple would result in U(VI)<sub>aq</sub> predominance (Figure 3.b).

In samples with < 1 µg U/L, U(IV)<sub>aq</sub> predominated, regardless of whether pe-values were obtained from the Fe- or S-redox couple. This suggests that redox systems are close to thermodynamic equilibrium in the samples with < 1 µg U/L. However, in groundwaters with > 20 µg U/L, the speciation of U<sub>aq</sub> was sensitive to whether pe-values were set by the Fe-couple (pe -5.0 to -4.4) or the S-couple (pe -4.0 to -3.8) for the PHREEQC calculations. This group had an important marine groundwater component and, therefore, contained bicarbonate (> 80 mg HCO<sub>3</sub><sup>-</sup>/L) in higher concentrations than the low U<sub>aq</sub> groundwaters. Groundwaters in thermodynamic equilibrium with pe-values > -4.0 should contain < 20% U(IV) if in thermodynamic equilibrium, but analytical determinations indicated that U(IV)<sub>aq</sub> comprised only 5% of the total U<sub>aq</sub> in KFM02A.3(500) (~150 µg U L<sup>-1</sup>; Suksi and Salminen, 2007). Therefore, the speciation of U<sub>aq</sub> in these groundwaters is in partial equilibrium with neither the Fe(II)/Fe(III) nor the S(-II)/S(VI) couple.

Total dissolved solids ranged 3 – 17 g/L but were typically 6 – 10 g/L (Table 1). Groundwaters were in equilibrium with barite and over-saturated or in equilibrium with calcite (Figure 4.a). Uranophane and haiweeite were strongly under-saturated in all groundwaters (Figure 4.b). Amorphous UO<sub>2.67</sub> (a mixed U(IV)/U(VI)-oxide) was slightly under-saturated or in equilibrium in most samples (Figure 4.c). Saturation indexes of U(IV)-bearing solids, such as amorphous coffinite and UO<sub>2</sub>·2H<sub>2</sub>O<sub>(am)</sub>, were sensitive to whether pe-values were fixed by Fe(II)/Fe(III) or S(-II)/S(VI). This implies that solid-phase U(IV) sinks are less effective at the mildly reducing pe-values determined by S(-II)/S(VI) than at the more

reducing pe-values determined from the Fe(II)/Fe(III) couple (Figure 4.d). Crystalline coffinite and uraninite were strongly oversaturated in all samples (not shown).

#### 4.2 Uranium isotopes and $U_{aq}$

Despite that depth and groundwater type should exert an important control on aqueous geochemistry, the  $[U_{aq}]$  was not related to either factor (Figure 5.a).  $[U_{aq}]$  was highest in the brackish-marine and glacial groundwaters ( $> 20 \mu\text{g} / \text{L}$ ), but these groundwaters had low  $U_{aq}$  ( $< 10 \mu\text{g} / \text{L}$ ) in other Forsmark borehole sections (Smellie et al., 2008). Maximum  $[U_{aq}]$  was found in KFM02A.3(500) (brackish-marine,  $150 \mu\text{g} / \text{L}$ ). The non-marine and most transition groundwaters, except for KFM03A.4(630), had low  $[U_{aq}]$ .

Since  $^{234}\text{U}$ , unlike  $^{238}\text{U}$ , is produced through alpha decay,  $U_{solid}$  preferentially releases  $^{234}\text{U}$  to the groundwater through alpha recoil, whereas soluble  $U_{solids}$  release both isotopes in an AR similar that of the precipitated phase. Therefore,  $[^{234}\text{U}/^{238}\text{U}]_{GW}$  reflects the contribution of  $U_{aq}$  from alpha recoil (from insoluble  $U_{solid}$  precipitates) versus mineral dissolution  $U_{aq}$ , which drive ARs toward  $> 1$  and  $< 1$ , respectively. In the Scandinavian Shield, reducing groundwaters that promote  $U_{solid}$  have  $[^{234}\text{U}/^{238}\text{U}]_{GW}$  of 3 to 7 (Suksi et al., 2006). At Forsmark and SFR the  $[^{234}\text{U}/^{238}\text{U}]_{GW}$  broadly ranged between 1.5 and 5.3 at intermediate depths (340 to 630 m.b.s.l.) but otherwise decreased toward depth (Figure 5.b). ARs in deep transition and non-marine groundwaters with  $< 5 \mu\text{g} \text{ U} / \text{L}$  were lower ( $2.4 \pm 0.4$ ) than typical Scandinavian Shield groundwaters. In general, groundwaters with  $> 20 \mu\text{g} \text{ U} / \text{L}$  had higher mean  $[^{234}\text{U}/^{238}\text{U}]_{GW}$  ( $3.3 \pm 1.3$ ) than the low  $[U_{aq}]$  waters, but ARs were low as 1.5 in  $U_{aq}$ -rich groundwaters at intermediate depth and  $\sim 2$  in the sample with  $150 \mu\text{g} / \text{L}$ . Other than rather low ARs in  $U_{aq}$ -rich groundwaters at intermediate-depth,  $[^{234}\text{U}/^{238}\text{U}]$  and  $[U_{aq}]$  showed no relation (Figure S1).

#### 4.3 Radium isotopes

##### 4.3.1 U-series: $^{223}\text{Ra}$ and $^{226}\text{Ra}$

Measured  $^{226}\text{Ra}_{GW}$  activities, reported in Table 2 alongside U and Rn activities, were similar to those extracted from the Sicada database. The  $^{226}\text{Ra}_{GW}$  increased towards depth in the bedrock (Figure 5.c). In North Carolina (USA), Vinson et al. (2009) attributed a similar trend to diminished Ra adsorption capacities in saline, chemically reducing groundwaters at depth. However, at Forsmark/SFR, the  $^{223}\text{Ra}_{GW}$  distribution was different than that of  $^{226}\text{Ra}_{GW}$ , which suggests that  $^{226}\text{Ra}_{GW}$  activities are not in steady state. Steady state is reached when the rates of  $\text{Ra}_{GW}$  supply (by recoil and production after decay of its Th-parent) and removal (by decay and precipitation) are equal and the activity of a specific isotope is temporally constant. Initially, a groundwater that flows into a new fracture environment, distinguished by a characteristic distribution of U-series isotopes, will have  $[^{223}\text{Ra}/^{226}\text{Ra}] \neq 0.046$  but will converge to the steady state AR of 0.046 after  $\sim 10,000$  years (Davidson and Dickson, 1986; Section 5.1).

Steady state  $^{223}\text{Ra}/^{226}\text{Ra}_{\text{GW}}$  prevailed in the oldest groundwaters, i.e. the non-marine groundwaters located in zones of low hydraulic conductivity (e.g. KFM01D.2(340), KFM03A.1(970)). In younger brackish marine and transition groundwaters that could contain elevated  $[\text{U}_{\text{aq}}]$ , the  $^{223}\text{Ra}/^{226}\text{Ra}_{\text{GW}}$  exceeded 0.046 ( $0.092 \pm 0.036$  and  $0.076 \pm 0.045$ , respectively). ARs were most variable in the SFR groundwaters that recently mixed with modern Baltic Sea water ( $0.25 \pm 0.25$ ; Section 2.1; Figure 5.d).

At Forsmark/SFR, the oldest groundwater is a saline, non-marine basement water with  $^{223}\text{Ra}/^{226}\text{Ra}_{\text{GW}} \sim 0.046$ , so an anti-correlation relation between  $^{223}\text{Ra}/^{226}\text{Ra}_{\text{GW}}$  and total dissolved solids (TDS) should reflect mixing between this component and the younger brackish waters. Such a relation was observed in the brackish-marine, transition, and non-marine groundwaters (Figure 6). However,  $^{223}\text{Ra}/^{226}\text{Ra}_{\text{GW}}$  were not related to TDS in the mixed SFR groundwaters due to the similarity in TDS between modern Baltic Sea water and the older, brackish Littorina mixtures. In the dilute glacial meltwaters, the  $^{223}\text{Ra}/^{226}\text{Ra}_{\text{GW}}$  were  $\sim 0.046$  but could be  $> 0.20$  where  $\text{TDS} > 5$  g/L, which probably reflects mixing between glacial and younger, marine groundwaters (Figure 6). The otherwise good agreement between  $^{223}\text{Ra}/^{226}\text{Ra}_{\text{GW}}$  and relative groundwater age justifies use of  $^{223}\text{Ra}/^{226}\text{Ra}_{\text{GW}}$  in residence time estimations at the site.

#### 4.3.2 Th-series: $^{224}\text{Ra}$ and $^{228}\text{Ra}$

$^{228}\text{Ra}$  and  $^{224}\text{Ra}$  can also reflect groundwater residence time because both are supplied by immobile  $^{232}\text{Th}$  and  $^{228}\text{Th}$  parents that are co-located in the bedrock (Figure 1; Tricca et al., 2000). The  $^{224}\text{Ra}/^{228}\text{Ra}_{\text{GW}}$  should reach steady state ( $0.67 - 1.5$ ) after 35 years ( $t_{1/2} \text{ } ^{228}\text{Ra} = 5.75$  y; Davidson and Dickson, 1986). The Forsmark/SFR  $^{224}\text{Ra}/^{228}\text{Ra}_{\text{GW}}$  should be in steady state but instead ranged  $0.12 - 9.4$  (Figure 5.f). Elsewhere, low  $^{224}\text{Ra}/^{228}\text{Ra}_{\text{GW}}$  have been attributed to mineral dissolution and diffusion of Ra from a matrix-bound Th-source to the well-head, which compared to alpha recoil or sorption, are slow processes that might release  $^{228}\text{Ra}$  over  $^{224}\text{Ra}$  due to the rapid decay of the latter (Hammond et al., 1988). At Forsmark/SFR, low ARs could be related to the distribution of  $^{232}\text{Th}_{\text{solid}}$ , found in metamict (urano)thorite grains that are readily leached by groundwater (Ewing et al., 1981; Cuney & Friedrich, 1987).

Three samples showed  $^{224}\text{Ra}/^{228}\text{Ra}_{\text{GW}} > 1.5$  together with high  $^{223}\text{Ra}/^{226}\text{Ra}_{\text{GW}}$ , of which only one was of the youngest, mixed SFR groundwater-type, the others being glacial and transition groundwaters (Section 2.1). These sections may be located at boundary between two groundwater mixtures, which fluctuates and continually resets the  $^{224}\text{Ra}/^{228}\text{Ra}_{\text{GW}}$ . For instance, the monitoring data from KFM03A.4(630) (transition,  $^{224}\text{Ra}/^{228}\text{Ra}_{\text{GW}} \sim 9$ ) shows clear, temporal variations in the brackish-marine and deep saline components (Figure S2). Similarly, the glacial groundwater KFR105.1(150) had  $^{224}\text{Ra}/^{228}\text{Ra}_{\text{GW}} 1.67 \pm 0.17$ , together with relatively high TDS and  $^{223}\text{Ra}/^{226}\text{Ra}_{\text{GW}}$  (Section 4.3.1) that likely reflect recent mixing with a younger, brackish groundwater. Despite that the construction of the SFR repository and associated

drawing down of Baltic Sea water occurred over 35 years ago, non-steady state [ $^{224}\text{Ra}/^{228}\text{Ra}$ ]<sub>GW</sub> may reflect a dynamic flow system in some areas.

#### 4.4 $^{222}\text{Rn}$

The daughter of  $^{226}\text{Ra}$ ,  $^{222}\text{Rn}$  is chemically inert and short-lived ( $t_{1/2} = 3.83$  d) and so reflects the surface area of  $U_{\text{solids}}$  in contact with the groundwater, a function of the  $U_{\text{solid}}$  concentration and fracture frequency. Since Forsmark  $^{222}\text{Rn}_{\text{GW}}$  activities exceeded  $^{238}\text{U}_{\text{GW}}$  and  $^{234}\text{U}_{\text{GW}}$  by several orders of magnitude ( $1.45 \cdot 10^5$  to  $4.44 \cdot 10^7$  dpm  $100\text{L}^{-1}$ ; Table 2),  $U_{\text{solid}}$  is more abundant in the fractures than is  $U_{\text{aq}}$ .

The  $^{222}\text{Rn}_{\text{GW}}$  and [ $U_{\text{aq}}$ ] were not correlated, except that groundwaters with  $< 5$   $\mu\text{gU/L}$  showed low  $^{222}\text{Rn}$  ( $3.2 \pm 1.9 \cdot 10^6$  dpm / 100 L), whereas groundwaters with higher [ $U_{\text{aq}}$ ] showed more variable  $^{222}\text{Rn}_{\text{GW}}$  ( $1.7 \pm 1.6 \cdot 10^7$  dpm / 100 L). The  $^{222}\text{Rn}_{\text{GW}}$  at Forsmark/SFR was similar to Laxemar, Sweden ( $9.8 \pm 15 \cdot 10^6$  dpm / 100 L; Grolander, 2009) and the Rolesville Granite in North Carolina, USA ( $2.0 \pm 1.5 \cdot 10^7$  dpm / 100 L; Vinson et al., 2009), so Forsmark has elevated [ $U_{\text{aq}}$ ] despite that its abundance of  $U_{\text{solid}}$  is average.

## 5 Discussion

### 5.1 Groundwater residence time

#### 5.1.1 Current limitations

The most prominent isotopes used to date groundwater include tritium,  $^{14}\text{C}$ ,  $^4\text{He}$ , and  $^{36}\text{Cl}$ . At Forsmark/SFR, tritium ( $t_{1/2}$  12.3 y) was used to trace the recent introduction of Baltic Sea water the mixed groundwaters, and the deep saline end-member was dated to  $>1.5$  Ma using  $^4\text{He}$  and  $^{36}\text{Cl}$  (Smellie et al., 2008). Littorina groundwaters were inferred to date back to  $\sim 6000$  y and so could only be dated using  $^{14}\text{C}$  ( $t_{1/2}$  5730 y), but calcite dissolution led to high uncertainties in the age calculations (Smellie et al., 2008). Given its 1600 y half-life,  $^{226}\text{Ra}$  could fill the age-dating gap for this coastal, Holocene groundwater system. Age constraints will elucidate the redox kinetics controlling [ $U_{\text{aq}}$ ] in the post-glacial groundwaters at Forsmark/SFR.

#### 5.1.2 A Bateman model to approximate residence time

Tritium,  $^{14}\text{C}$ , and  $^{36}\text{Cl}$ , are atmospherically-sourced and so reflect groundwater age, i.e. the time elapsed since a parcel of surface water entered the subsurface. However,  $\text{Ra}_{\text{GW}}$  is sourced by aquifer solids and so reflects a groundwater's residence time, i.e. the time elapsed since the sampled groundwater entered its current fracture environment, characterized by a specific U- or Th-series isotope distribution that controls the steady state activity of  $\text{Ra}_{\text{GW}}$  (Section 4.3.1-.2).

Like most other groundwater constituents, U- and Th-series isotopes can be supplied to or removed from the groundwater in a given fracture section through advection, weathering/precipitation of host rock minerals, and desorption from/adsorption to fracture surfaces. Most groundwater constituents temporally

evolve according to groundwater flow rates and geochemical reaction kinetics. However,  $Ra_{GW}$  is also influenced by radioactive decay, of dissolved parents and parents mineralized in or adsorbed to the aquifer host rock that recoil radium atoms into the groundwater, as well as its own decay, which removes Ra from the groundwater. Like these processes, the rates of  $Ra_{GW}$  supply and removal are dependent on the decay constants of radium isotopes and their progenitors. Porcelli (2008) capture the re-equilibration of isotope  $i_w$ , a U- or Th-series daughter in groundwater that has entered a fracture environment with a distinct U- or Th-series isotope distribution, by Equation 1, whose terms and variables are explained above and defined Table 3.

### Equation 1:

$$\frac{di_w}{dt} = v \left( \frac{di_w}{di_x} \right) + bw_i i_R + b\epsilon_i \lambda_P P_R + (f_i \lambda_P P_{ads} + \lambda_P P_W) - Q_i i_w - \lambda_i i_w (1 + K_i)$$

If Equation 1 can be solved for time,  $t$ , then it will be possible to calculate the period of time taken for the groundwater to acquire the observed  $Ra_{GW}$  signature, or, the groundwater residence time. The large number of unknown variables obstructs the resolution of Equation 1, but here, we discuss a series of simplifying assumptions, listed in Table 3, that enable a direct, numerical solution. For instance, the rate of short-lived  $^{223}Ra$  and  $^{224}Ra$  decay is fast relative to the rate of local groundwater flow and to the kinetics of Ra-bearing mineral precipitation/dissolution. Since these isotopes will decay before they are subject to advection, weathering, or precipitation, the  $v \left( \frac{di_w}{di_x} \right)$ ,  $bw_i i_R$ , and  $-Q_i i_w$  terms can be eliminated from Equation 1. Furthermore, the three terms that reflect the  $Ra_{GW}$  contribution from local solid- and aqueous-phase parents can be combined into one term,  $\lambda_P P_{R+W}$ . Finally, the dimensionless partition coefficient  $K_i$ , defined as the ratio of  $i$  atoms adsorbed to atoms in solution, is temporarily replaced with  $\frac{i_{ads}}{i_w}$ . This will simplify integration of Equation 2, which also considers the afore-listed assumptions:

### Equation 2

$$\frac{di_w}{dt} = \lambda_P P_{R+W} - \lambda_i i_w \left( 1 + \frac{i_{ads}}{i_w} \right) = \lambda_P P_{R+W} - \lambda_i i_w - \lambda_i i_{ads}$$

Rearranging Equation 2 facilitate its integration:

### Equation 3

$$\int \frac{di_w}{\left( -\frac{\lambda_P P_{R+W}}{\lambda_i} + i_w + i_{ads} \right)} = \int -\lambda_i dt$$

1 Integration of Equation 3 yields:

2 **Equation 4**

$$3 \quad -\frac{\lambda_P P_{R+W}}{\lambda_i} + i_w + i_{ads} = C e^{-\lambda_i t}$$

4 Equation 4 is multiplied by  $\lambda_i$  to obtain  $\lambda_i i_w + \lambda_i i_{ads}$ , which can then be simplified to  $\lambda_i i_w (1 + K_i)$ :

5 **Equation 5**

$$6 \quad -\lambda_P P_{R+W} + \lambda_i i_w (1 + K_i) = \lambda_i C e^{-\lambda_i t}$$

7 We derive a value for  $C$ , the constant of integration, by setting  $i_w = 0$  at  $t_0$ . This is conceptually equivalent  
 8 to assuming that groundwater entering the sampled fracture environment is radium-free ( $Ra_{GW} = 0$  at  $t =$   
 9  $0$ ). This assumption is valid for short-lived  $^{223}Ra$ ,  $^{224}Ra$ , and  $^{228}Ra$ , which slow-flowing deep groundwater  
 10 will not transport far from their source. Thus, when  $i_w = ^{223}Ra_{GW}$ ,  $^{224}Ra_{GW}$ , and  $^{228}Ra_{GW}$ ,  $C = -\frac{\lambda_P P_{R+W}}{\lambda_i}$   
 11 can be substituted into Equation 5, which is then rearranged to equal the groundwater activity of isotope  $i$ :

12 **Equation 6**

$$13 \quad \lambda_i i_w = \frac{\lambda_P P_{R+W} (1 - e^{-\lambda_i t})}{(1 + K_i)}$$

14 We note that longer-lived  $^{226}Ra$  may be subject to advection, thereby permitting initial  $^{226}Ra_{GW} > 0$  in  
 15 groundwater flowing between distinct fracture environments. This scenario would invalidate our  
 16 assumption and is discussed more extensively in Section 5.1.3.

17 One of few remaining unknowns, the partition coefficient  $K_i$  will be the same for all radium isotopes due  
 18 to their identical chemical properties. Since  $K_{^{223}Ra} \sim K_{^{224}Ra} \sim K_{^{226}Ra} \sim K_{^{228}Ra} = K_{Ra}$ , applying Equation 6 to  
 19 two radium isotopes and converting the left-side of the equation to an AR will eliminate  $K_{Ra}$  from the  
 20 equation:

21 **Equation 7**

$$22 \quad \frac{\lambda_{^{223}Ra} ^{223}Ra_w}{\lambda_{^{226}Ra} ^{226}Ra_w} = \frac{\lambda_{^{227}Th} ^{227}Th_{R+W} (1 - e^{-\lambda_{^{223}Ra} t})}{\lambda_{^{230}Th} ^{230}Th_{R+W} (1 - e^{-\lambda_{^{226}Ra} t})}$$

23 According to Equation 7, the radium decay constants will govern the temporal evolution of the  
 24 groundwater AR, which has an initial value of zero but converges toward that supported through decay of  
 25 the adsorbed/mineralized and dissolved parents with increasing time.

Working in ARs also precludes the need to know the bulk activity of local parents in the aquifer. Since  $^{235}\text{U}$  and  $^{238}\text{U}$  are chemically identical, they do not fractionate from each other and so are co-located throughout the bedrock in  $[\text{}^{235}\text{U}/\text{}^{238}\text{U}]_{\text{rk}}$  AR of 0.046 (e.g. Davidson & Dickson, 1986). The progeny in their chains also exhibit similar chemical behavior and so will likewise persist throughout the host rock in an AR of 0.046 (Porcelli, 2008), which is assigned to the coefficient on the right-hand side of Equation 7:

#### Equation 8

$$\frac{\lambda_{223\text{Ra}}^{223}\text{Ra}_w}{\lambda_{226\text{Ra}}^{226}\text{Ra}_w} = 0.046 * \frac{(1 - e^{-\lambda_{223\text{Ra}}t})}{(1 - e^{-\lambda_{226\text{Ra}}t})}$$

We solve Equation 8 by substituting a range of values, equally spaced between 0 and 10,000 y, for  $t$ , and then calculating the  $[\text{}^{223}\text{Ra}/\text{}^{226}\text{Ra}]_{\text{GW}}$  AR for each time-step. A similar approach, discussed in Appendix 1, is used to understand the progression of  $[\text{}^{224}\text{Ra}/\text{}^{228}\text{Ra}]_{\text{GW}}$  toward steady-state values. Then, to compare the evolution of these two ARs, the resulting  $[\text{}^{223}\text{Ra}/\text{}^{226}\text{Ra}]_{\text{GW}}$  vector was plotted against that of the  $[\text{}^{224}\text{Ra}/\text{}^{228}\text{Ra}]_{\text{GW}}$  (purple curve in Figure 7). Each point along the generated curve represents a potential  $[\text{}^{223}\text{Ra}/\text{}^{226}\text{Ra}]_{\text{GW}}$ -  $[\text{}^{224}\text{Ra}/\text{}^{228}\text{Ra}]_{\text{GW}}$  combination for a point in time following introduction of the sampled groundwater to its present fracture environment. ARs at  $t = 1, 10, 100, 1000$ , and 10,000 y are marked along the curve, showing that  $[\text{}^{224}\text{Ra}/\text{}^{228}\text{Ra}]_{\text{GW}}$  reaches steady state more rapidly than does  $[\text{}^{223}\text{Ra}/\text{}^{226}\text{Ra}]_{\text{GW}}$ , as controlled by the respective  $^{228}\text{Ra}$  and  $^{226}\text{Ra}$  half-lives of 5.75 and 1600 y. Forsmark/SFR groundwater residence times can be assessed from the position of the measured  $[\text{}^{223}\text{Ra}/\text{}^{226}\text{Ra}]_{\text{GW}}$  along the curve (Figure 7).

#### 5.1.3 Model verification

The Bateman model described above relies on several assumptions that do not resonate in every groundwater environment. For instance, the long half-life of  $^{226}\text{Ra}$  may, under certain geochemical conditions, undermine the assumption that dissolution/precipitation reactions have a negligible impact on  $\text{Ra}_{\text{GW}}$ . Martin and Akber (1999) found  $[\text{}^{223}\text{Ra}/\text{}^{226}\text{Ra}] > 0.046$  in groundwaters that were supersaturated with respect to barite, which is not the case in Forsmark/SFR groundwaters (Figure 5). Furthermore, barite was scarce in the fracture fillings recovered from SKB drillcores (Sandström et al., 2008). Therefore, co-precipitation of  $\text{Ra}_{\text{GW}}$  in barite probably does not disrupt the  $[\text{}^{223}\text{Ra}/\text{}^{226}\text{Ra}]_{\text{GW}}$  at Forsmark/SFR.

Significant advection of  $^{235}\text{U}$ - and  $^{238}\text{U}$  series nuclides may also undermine the assumption of initial  $i_w = 0$  (at  $t = 0$ ). In the case of appreciable and recent uranium advection, it may not be reasonable to assign a value of 0.046 to the AR of  $^{223}\text{Ra}$  and  $^{226}\text{Ra}$  progenitors (Equations 7, 8). If uranium-rich groundwaters are depleted in particle-reactive  $^{231}\text{Pa}$  and  $^{230}\text{Th}$ , then these intermediate nuclides must be replenished

before  $^{223}\text{Ra}$  and  $^{226}\text{Ra}$  can regrow into solution. In this case, the temporal evolution of  $[\text{}^{223}\text{Ra}/\text{}^{226}\text{Ra}]_{\text{GW}}$  will be influenced by the decay constants of the parent isotopes, thereby extending the time required for the AR to reach a steady state AR of 0.046. Advection of  $^{226}\text{Ra}_{\text{GW}}$  is another scenario that may lead to initial  $i_w > 0$  and thereby affect the constant of integration,  $C$ , that was substituted into Equation 6.

Although this study was motivated by the occurrence of elevated  $[\text{U}_{\text{aq}}]$  in some Forsmark groundwaters, uranium advection is unlikely to affect local  $[\text{}^{223}\text{Ra}/\text{}^{226}\text{Ra}]_{\text{GW}}$ . The  $[\text{}^{222}\text{Rn}/\text{}^{234}\text{U}]_{\text{GW}} \gg 1$  (Table 2) indicate that U-series parents in the local bedrock are a more significant source of  $\text{Ra}_{\text{GW}}$  than the dissolved uranium fraction. Furthermore, fracture analyses showing  $[\text{}^{234}\text{U}/\text{}^{238}\text{U}]_{\text{rk}}$  and  $[\text{}^{230}\text{Th}/\text{}^{234}\text{U}]_{\text{rk}}$  of  $\sim 1$  (Sandström et al., 2008) support the assumption that  $^{238}\text{U}$ - and  $^{235}\text{U}$ -series isotopes co-occur in an AR of 0.046 at Forsmark (Equations 7, 8). Nevertheless, an approach to simulating the evolution of  $[\text{}^{223}\text{Ra}/\text{}^{226}\text{Ra}]_{\text{GW}}$  for initial disequilibrium in the uranium-series parents is presented in Appendix 1.

Since the possibility that initial  $^{226}\text{Ra}_{\text{GW}} > 0$  in the heterogenous Forsmark flow system cannot be ruled out, Appendix 1 also describes an approach to testing the sensitivity of the derived  $[\text{}^{223}\text{Ra}/\text{}^{226}\text{Ra}]_{\text{GW}}$  to initial  $^{226}\text{Ra}_{\text{GW}}$  values. The results indicate that Equation 8 does not capture an accurate residence time for a groundwater that supports lower  $\text{Ra}_{\text{GW}}$  than its previous environment. Here, the AR will be  $< 0.046$  until  $^{226}\text{Ra}_{\text{GW}}$  stabilizes after  $\sim 10,000$  y (red curve in Figure 7). The poor agreement between ARs for timesteps preceding 1000 y suggest that Equation 8 will also produce inaccurate residence times for the mixed-type SFR groundwaters, which are younger than 100 y according to tritium isotope analyses (Figure 7; Nilsson et al., 2011).

Nevertheless, for the three curves simulating groundwater that has entered a fracture that supports  $\text{Ra}_{\text{GW}}$  exceeding that of the previous groundwater environment, the  $[\text{}^{223}\text{Ra}/\text{}^{226}\text{Ra}]_{\text{GW}}$  curves converge at  $\text{AR} = 0.12$  after 1000 years (purple, blue, and orange curves in Figure 7). This demonstrates that groundwater that entered a  $\text{U}_{\text{solid}}$ -rich fracture at any point between 1000 and 10,000 years ago will have  $[\text{}^{223}\text{Ra}/\text{}^{226}\text{Ra}]_{\text{GW}}$  between 0.046 and 0.12, independent of the initial  $^{226}\text{Ra}_{\text{GW}}$ . The brackish-marine and transition groundwaters at Forsmark fall within this range. These groundwaters were challenging to date using  $^{14}\text{C}$ , but the 1000-10,000 y age range derived from the  $[\text{}^{223}\text{Ra}/\text{}^{226}\text{Ra}]$  model is consistent with the timing of the Littorina Sea transgression (8000 – 2000 BP; Röbller, 2006). The  $[\text{}^{223}\text{Ra}/\text{}^{226}\text{Ra}]_{\text{GW}}$  age of  $> 10,000$  y also consistent with the background knowledge of the non-marine groundwaters, which are older than 1.5 My according to the  $^4\text{He}$  and  $^{36}\text{Cl}$  isotope systems (Smellie et al., 2008). Therefore, Equation 8 seems to provide reliable age constraints for groundwater that entered its present residence, in a  $\text{U}_{\text{solid}}$ -rich fracture zone, over 1000 years ago.

#### 5.1.4 Residence times and redox kinetics

The residence time constraints have implications on the stability, and therefore the origin, of Forsmark  $U_{aq}$ . The oldest, non-marine and transition groundwater-types, showed similarly high  $U(IV)_{aq}$  proportions regardless of which redox couple was used for the thermodynamic calculation (Section 4.1; Figure 3). Considered alongside the low  $[U_{aq}]$  in these waters, these redox systems are near thermodynamic equilibrium.

In the two marine-influenced groundwater mixtures, the calculated  $U_{aq}$  speciation—much like the  $[U_{aq}]$ —varies dramatically, depending on whether the pe-value is fixed by the Fe(II)/Fe(III) or S(-II)/S(VI) redox couple (Section 4.1). For both the modern, mixed Baltic SFR and the ancient, brackish marine-Littorina Forsmark waters, the uranium and sulfur redox systems showed similarly large deviations from thermodynamic equilibrium with the iron redox system, despite that the  $[^{223}Ra/^{226}Ra]_{GW}$  reflect ages of less than 100 years and several thousand years for the respective groundwater-types (Section 5.1.3; Figure 7). Therefore, the evolution to thermodynamic equilibrium is kinetically inhibited in the ancient, bicarbonate-rich waters. Identifying the geochemical limitations in the system is necessary to understand the the processes controlling the  $[U_{aq}]$ .

Near-surface groundwater systems contain organic carbon, which can support active microbial communities that mediate redox reactions and, thereby, facilitate U(VI) reduction (e.g. Belli et al., 2015). Since the Forsmark groundwaters are depleted in organic carbon (typically < 0.3 mM; Tullborg et al., 2010), the growth of these bacteria—and therefore U(VI) reduction—might be inhibited, although microbial communities are not invariably small throughout the Forsmark system (Hallbeck & Pedersen, 2012). In addition to microbial cell count, the kinetics of U(VI) reduction varies according to pH, Eh, alkalinity, and  $Ca^{2+}$  conditions, such that reduction rates are relatively slow in  $Ca_2UO_2(CO_3)_3^0$ -dominated systems (Sheng et al., 2011; Stewart et al., 2011; Ulrich et al., 2011). The lowest reported rate constant for a  $Ca_2UO_2(CO_3)_3^0$ -dominated system, fed by microbial lactate digestion, is  $3.1 \cdot 10^{-7} \text{ s}^{-1}$  (Stewart et al., 2011). Reduced at this rate,  $[U_{aq}]$  would decrease by two orders-of-magnitude  $[U_{aq}]$  within a year, whereas  $[U_{aq}]$  at Forsmark has been stable since 2008 (Tullborg et al., 2017).

Since Fe(II) represents thermodynamic driver for  $U(VI)_{aq}$  reduction in the Forsmark groundwaters (Figure 3.a), the  $[U_{aq}]$  might be related to slow reduction kinetics that, in turn, are a consequence of the diminished microbial activity or of the behaviour of the  $Ca_2UO_2(CO_3)_3^0$  complex itself. Electron transfer from Fe(II), through both abiotic (Taylor et al., 2015) and direct, microbial (e.g. Stewart et al., 2011) pathways, is promoted by adsorption of U(VI) to a mineral surface or cell membrane. Since these are negatively charged, the low affinity of the neutral  $Ca_2UO_2(CO_3)_3^0$  complex for both substrates (Fox et al.,

2006; Sheng & Fein, 2014) could explain its persistence in the deep groundwaters. Nevertheless, a purely kinetic explanation for the  $[U_{aq}]$  implies that reduction rates in the the ancient groundwaters are several orders-of-magnitude lower than have been—or can be—observed in laboratory experiments.

S(-II) is a stronger reductant than ferrous iron, but its concentrations are too low to thermodynamically drive reduction of  $U(VI)_{aq}$  in the  $Ca_2UO_2(CO_3)_3^0$ -dominated groundwaters of glacial and marine origin (Figure 3.b). Except for one sample that was disrupted less than thirty years ago ( $[^{224}Ra/^{228}Ra] \gg 1.5$ ; KFM03A.4(630)), calculations performed using S(-II)/S(VI) pe-values indicate that U(VI) is thermodynamically stable in Forsmark/SFR groundwaters with  $[U_{aq}] > 5 \mu g/L$ . Redox disequilibrium between the Fe(II)/Fe(III) and S(-II)/S(VI) couple could be attributed to low populations of sulfate reducing bacteria that could otherwise reduce U(VI) through  $HS^-$  generation. Therefore, limited microbial activity may influence  $U(VI)_{aq}$ , albeit indirectly, by controlling sulfate reduction.

If subject to oxidation by glacial meltwater, then the groundwaters would need to retain  $U(VI)_{aq}$  over geologic time, and the  $[U_{aq}]$  would be primarily explained by slow reduction kinetics in the  $Ca_2UO_2(CO_3)_3^0$ -predominated system. This scenario would entail uniformly high  $[U_{aq}]$  throughout groundwaters of a shared origin, with the ancient, brackish-marine groundwaters showing lower  $[U_{aq}]$  than the younger, mixed SFR groundwaters. Given that the  $[U_{aq}]$  follows a more complex distribution, the system may, instead, be explained by on-going interactions between  $U(VI)_{solids}$  and mildly reducing groundwaters wherein U(VI) reduction is inhibited. This alternative, supported by the apparent intricacies of the redox system, would better explain the orders-of-magnitude variation in  $[U_{aq}]$  throughout the ancient, brackish-marine groundwaters (Figures 3, 7). Whether the  $U(VI)_{solid}$  sources formed in response to oxidation by glacial meltwater will be further explored through geochemical modelling and U-/Th-series isotope ARs.

## 5.2 Geochemical modelling

### 5.2.1 Redox behavior of uranium

Updated geochemical models now incorporate thermodynamic data for the  $Ca_2UO_2(CO_3)_3^0$  and  $CaUO_2(CO_3)_3^{-2}$  complexes, which was lacking in the database used for the previous Forsmark/SFR speciation-solubility calculations. The initial results suggested that  $U(IV)_{aq}$  predominated at pe-values lower than  $-3.3$ , even in bicarbonate-rich groundwaters (Gimeno et al., 2007). Thus, the solubility of  $U(VI)_{aq}$  in these groundwaters, which have pe-values  $< -3.7$ , was previously underestimated and so indicated that  $[U_{aq}]$  was exceptionally high. However, calculations using the updated database show that  $U(VI)_{aq}$  predominates at pe-values as low as  $-4.5$  if alkalinity and Ca concentrations are  $>100$  and  $>1000$  mg/L, respectively (Figure 8.a).

Sensitivity analyses further suggest that the stability of  $U(VI)_{aq}$  varies dramatically across the prevalent range of Forsmark/SFR groundwater compositions (Figure 8). To determine which geochemical constituents have the most significant implications for the local uranium redox system, we systematically varied the value of individual components (i.e. pe-value, alkalinity, and calcium concentration) over the range observed at Forsmark/SFR while keeping constant values for all other elements in the KFM02A.3(500) dataset. Between pe-values of  $-4.6$  and  $-4.0$ , predominance rapidly shifts from  $U(IV)_{aq}$  to  $U(VI)_{aq}$  (Figure 8.a), and consequently decreases the saturation indexes of  $U_{solid}$  sinks (e.g. coffinite<sub>(am)</sub> and  $UO_2 \cdot 2H_2O_{(am)}$ ). High alkalinity and Ca concentrations ( $> 60$  mg  $HCO_3^-/L$  or  $> 400$  mg  $Ca^{2+}/L$ ) can also promote  $U(VI)_{aq}$  predominance, as  $Ca_2UO_2(CO_3)_3^0$ , in a mildly reducing regime (pe-value  $-4.4$ ; Figure 8.b-c).

The present models indicate that, depending on the precise pe-value, alkalinity, and Ca concentration,  $U(VI)_{aq}$  may actually be stable in some of the local groundwaters. The rapid shift in  $U_{aq}$  speciation across the relevant compositional ranges, from insoluble  $U(IV)$  to soluble  $U(VI)$ , may partially explain the observed  $[U_{aq}]$  distribution. This observation supports the hypothesis that local  $U_{aq}$  is governed by on-going water-rock interaction. On-going water-rock interaction was also inferred from the residence time calculations (Section 5.1.4) and better accounts for the variability in  $[U_{aq}]$  throughout the groundwaters (Section 2.2.) than the scenario of long-term  $U_{aq}$  retention following oxidation by glacial meltwater.

Nevertheless, the groundwater must be in contact with a soluble  $U(VI)_{solid}$  source for  $U(VI)_{aq}$  complexes to form. Identification of this source will provide insight into the timing of its formation, i.e. during geologically early versus post-glacial oxidizing conditions and will be guided by forward modelling,  $Ra_{GW}$  results, and background studies of Forsmark uranium minerals (Krall et al., 2015, 2019).

### 5.2.2 Identifying $U_{aq}$ sources and sinks using forward modelling

Potential sources of  $U(VI)$  include local Ca- $U(VI)$ -silicate minerals (haiweeite and uranophane) and fine-grained  $UO_{2+x}$  (Section 2.3; Krall et al., 2015). During the Proterozoic, hydrothermal fluids partially oxidized the  $U(IV)$  in uraninite and uranothorite to  $U(VI)$ , which precipitated in the haiweeite and uranophane that produced Proterozoic and Palaeozoic Pb-Pb ages (Krall et al., 2019) and, at present, are scattered throughout pegmatites in the deformation zones. More recently, some of the Ca- $U(VI)$ -silicates were altered by carbonate-rich fluids ( $< 100$  Ma), and  $UO_{2+x}$  precipitated around Fe-bearing minerals on fracture surfaces (Palaeozoic or younger; Krall et al., 2019). In the  $UO_{2+x}$ , PbO concentrations were too low to provide for Pb-Pb dating (Krall et al., 2015; 2019) and  $U(IV)/U(VI)$  proportions were uncertain. Therefore, the  $UO_{2+x}$  phase found in thin sections was young, but its role in on-going water-rock interaction, i.e. as a source of  $U(VI)$  or a sink for  $U(IV)$ , is unclear.

In order to determine whether uranophane or  $\text{UO}_{2+x}$  is a more likely source of  $\text{U(VI)}_{\text{aq}}$ , PHREEQC dissolution models were constructed for each mineral. The “ $\text{UO}_{2.67}$ ” dissolution model emulates a scenario wherein the  $\text{UO}_{2+x}$  phase has a high proportion of U(VI) and so represents a  $\text{U(VI)}_{\text{aq}}$  source that precipitated from oxidizing, post-glacial waters. Alternatively, large proportions of U(IV) in the observed  $\text{UO}_{2+x}$  would implicate its role as a uranium sink. To clarify whether such a  $\text{U(IV)}_{\text{solid}}$  is precipitating from uranophane or  $\text{UO}_{2.67}$ , an additional simulation was constructed for each U(VI)-mineral, wherein amorphous “ $\text{UO}_2 \cdot 2\text{H}_2\text{O}$ ” was designated as an “equilibrium phase.”

Whether uranophane or  $\text{UO}_{2.67}$  is the more likely  $\text{U(VI)}_{\text{aq}}$  source is important to determine because uranophane dissolution could proceed simply given the presence of geologically old Ca-U(VI)-silicates. If young,  $\text{UO}_{2.67}$  is a more likely  $\text{U(VI)}_{\text{aq}}$  source, this would provide evidence in support of the post-glacial oxidation hypothesis.

Groundwater chemistry from KFM02A.3(500) was modelled, except that the observed  $150 \mu\text{gU/L}$  was adjusted to be in equilibrium with  $\text{UO}_{2(\text{am})}$  at the start of the simulation so as to reflect the solubility calculation results (not shown). For both models (i.e. with and without the  $\text{UO}_2 \cdot 2\text{H}_2\text{O}$  equilibrium phase), step-wise uranophane dissolution supports higher  $[\text{U}_{\text{aq}}]$  than does  $\text{UO}_{2.67}$  dissolution (Figure 9). In the model that accounted for precipitation of  $\text{UO}_2 \cdot 2\text{H}_2\text{O}$ , dissolution of  $\text{UO}_{2.67}$  drives a very limited increase in  $[\text{U}_{\text{aq}}]$  (“ $\text{UO}_2 \cdot 2\text{H}_2\text{O}$  eq” in Figure 9). Therefore, the younger and less soluble  $\text{UO}_{2+x}$  phases are likely to serve as a  $\text{U}_{\text{aq}}$  sink, as opposed to a  $\text{U(VI)}_{\text{aq}}$  source that formed from oxidizing glacial meltwater. Compared to  $\text{UO}_{2.67}$ , groundwater interaction with Ca-U(VI)-silicate minerals, dated to the Proterozoic, seems to promote conspicuously high  $[\text{U}_{\text{aq}}]$ .

Textural and isotopic observations of recent interactions between Ca-U(VI)-silicates and bicarbonate-rich fluids (Krall et al., 2015, 2019) corroborate the interpretation that  $\text{U}_{\text{aq}}$  is related to the presence of these minerals at Forsmark/SFR. Given these PHREEQC results, the variability in  $[\text{U}_{\text{aq}}]$  throughout the groundwaters (Section 2.2) can be attributed to:

1. the  $\text{U}_{\text{aq}}$  speciation is sensitive across the observed range of groundwater redox, alkalinity, and Ca concentrations and can be predominated by the aqueous  $\text{Ca}_2\text{UO}_2(\text{CO}_3)_3^0$  complex that inhibits uranium precipitation.
2. the sporadic distribution of soluble Ca-U(VI)-silicates, which tend to occur in U-rich, hydrothermally-altered pegmatites.

Although high  $[U_{aq}]$  can be explained without a recent oxidation event, the geochemical modelling results cannot preclude the possibility Holocene U(VI) is supplied to the groundwater by a  $UO_{2.67}$ -like phase. Thus, U- and Th-series isotopes are employed to further probe the mineralogic source of  $U(VI)_{aq}$ .

### 5.3 *U/Th rock ratios provided by Ra isotopes*

The short half-lives of  $Ra_{GW}$  isotopes prevent their long-range advection, so the  $Ra_{GW}$  signature is inherited from the wall rock on a local scale. Two radium isotopes are generated from each natural uranium and thorium, and their groundwater ARs reflect that of the nearest few meters of rock that comprises the fracture surface. Thus, for a groundwater with a specific  $U_{aq}$  speciation and concentration, the  $Ra_{GW}$  can be used to characterize the chemical composition of the nearby fracture surface. The  $[^{226}Ra/^{228}Ra]_{GW}$  is typically used to determine the AR of the nearby rock ( $[^{238}U/^{232}Th]_{solid}$ ) (e.g. Porcelli 2008; Krishnaswami et al., 1982, Vengosh et al., 2009, Tomita et al., 2014), but  $[^{223}Ra/^{228}Ra]_{GW}$  is preferred at Forsmark and SFR due to the non-steady state  $^{226}Ra_{GW}$ . For groundwaters with non-steady state  $^{228}Ra_{GW}$  ( $[^{224}Ra/^{228}Ra]_{GW} > 1.5$ ; Section 4.3.2), the  $[^{223}Ra/^{224}Ra]_{GW}$  is substituted.

Like their  $^{235}U$  and  $^{238}U$  parents,  $^{223}Ra$  is less abundant than  $^{226}Ra$ , so the  $[^{223}Ra/^{228}Ra]_{GW}$  should be corrected using the natural  $[^{235}U/^{238}U]$  of 0.046 in order to determine the  $[^{238}U/^{232}Th]_{solid}$  (Eqn. 4):

#### Equation 4:

$$\frac{^{223}Ra}{^{228}Ra}_{GW} \times \frac{1}{0.046} = \frac{^{223}Ra}{^{228}Ra}_{corr} \approx \frac{^{238}U}{^{232}Th}_{solid}$$

The  $[^{223}Ra/^{228}Ra]_{GW}$  at Forsmark/SFR ranged 0.018 to 0.92, which is equivalent to a  $[^{223}Ra/^{228}Ra]_{corr}$  or  $[^{238}U/^{232}Th]_{solid}$  range of 0.38 to 20 (Eqn. 3). The mean and median  $[^{223}Ra/^{228}Ra]_{corr}$  (4.1 and 2.9, respectively) are similar to those reported from other crystalline terrains.  $[^{226}Ra/^{228}Ra]_{GW}$  ranges 4.8 – 7.7 at Stripa, Sweden (Andrews et al., 1989), 0.2 – 75 throughout Finland (Asikainen & Kahlos 1979; Asikainen, 1981), and 0.2 – 7 elsewhere (Vinson et al., 2009; Tomita et al., 2010, 2016).

Results from analysis of fracture filling chemistry, converted to ARs, also suggest that Forsmark and SFR fracture surfaces ( $>3.0$  but rarely  $>30$   $[^{238}U/^{232}Th]_{solid}$ ) are modestly  $U_{solid}$ -enriched, compared to the bedrock background of 0.30 – 3.0  $[^{238}U/^{232}Th]_{solid}$  (Sandström et al., 2008; Nilsson et al., 2011; Sandström & Tullborg, 2011).  $U_{solid}$ -rich pegmatites are also more enriched than the bedrock ( $[^{238}U/^{232}Th]_{solid} = 1.4 – 31$ ; Krall et al., 2015).

The  $[^{223}Ra/^{228}Ra]_{corr}$  are of the same order of magnitude as  $[^{238}U/^{232}Th]_{solid}$ , but where both groundwater- and solid-based analyses are available from the same fracture zone, minor discrepancies in AR are apparent. Fracture mineral chemistry indicates that the Forsmark fractures, sampled from depths  $> 400$

m., have higher and more variable  $[^{238}\text{U}/^{232}\text{Th}]_{\text{solid}}$  than the SFR fractures, representing depths of 200 – 400 m. (Nilsson et al., 2011; Sandström & Tullborg, 2011), but the  $[^{223}\text{Ra}/^{228}\text{Ra}]_{\text{corr}}$  ( $2.3 \pm 1.9$  and  $5.4 \pm 5.9$ , respectively) suggest the opposite case. Furthermore, fractures that showed  $[^{238}\text{U}/^{232}\text{Th}]_{\text{solid}}$  enrichments do not have particularly high  $[^{223}\text{Ra}/^{228}\text{Ra}]_{\text{corr}}$ . For instance, the maximum  $[^{238}\text{U}/^{232}\text{Th}]_{\text{solid}}$  (~1070) was collected from the vicinity of the KFM03A.4(630) groundwater, which had lower  $[^{223}\text{Ra}/^{228}\text{Ra}]_{\text{corr}}$  (6.6) than several SFR groundwaters (>10). This divergence is attributed to the different surface areas captured by the  $\text{Ra}_{\text{GW}}$  and the fracture solids, recovered from drill cores (several meters versus ~20 cm<sup>2</sup>, respectively).

Ultimately, the low median  $[^{223}\text{Ra}/^{228}\text{Ra}]_{\text{corr}}$  of 2.9 suggests that, rather than the  $\text{U}_{\text{solid}}$ -enriched fracture surfaces, the metagranite and/or pegmatite rock matrix dominate water-rock interaction at Forsmark and SFR. Andrews et al. (1989) arrived at a similar conclusion from  $[^{226}\text{Ra}/^{228}\text{Ra}]_{\text{GW}}$  analysis at Stripa, Sweden.

#### 5.4 $[^{223}\text{Ra}/^{228}\text{Ra}]_{\text{corr}}$ and uranium sources

Uranium-series isotopes have been used to locate redox fronts in both sedimentary and crystalline terrains (e.g. Cowart, 1980; Osmond et al., 1983; Osmond & Cowart, 1992; MacKenzie et al., 1992; Drake et al., 2009). A redox front can form after surface water recharges an aquifer and oxidizes the nearby  $\text{U}_{\text{solid}}$ , which is thereafter transported as  $\text{U}_{\text{aq}}$  until the groundwater becomes anoxic. At this point, a uranium deposit forms, marking the transition to reducing conditions. Using activities of  $^{238}\text{U}$ ,  $^{234}\text{U}$ , and  $^{230}\text{Th}$  on fracture surfaces, Drake et al. (2009) detected a redox front at a depth of 30 m at the Laxemar site in southeast Sweden. However, the same method did not reveal a redox front at Forsmark, and this was attributed to the subhorizontal orientation of fractures in the uppermost 400 m of bedrock Sandström et al. (2008). Nevertheless, to locate a palaeoredox front at Forsmark could provide evidence for or against a recent oxidation of  $\text{U}_{\text{solid}}$  at depth.

Osmond et al. (1983) modelled the evolution of  $[^{234}\text{U}/^{238}\text{U}]_{\text{GW}}$  and  $[\text{U}_{\text{aq}}]$  across a redox front and found that low ARs are associated with leaching of  $\text{U}_{\text{solid}}$  and high ARs with  $\text{U}_{\text{solid}}$  precipitation. Within the redox front,  $[\text{U}_{\text{aq}}]$  can be high and show a range of ARs (Figure 10.a). No such curve between  $[^{234}\text{U}/^{238}\text{U}]_{\text{GW}}$  and  $[\text{U}_{\text{aq}}]$  was evident in Forsmark groundwater analyses (Figure S1).

$\text{Ra}_{\text{GW}}$  is seldomly applied to redox front studies, despite that the  $[^{226}\text{Ra}/^{228}\text{Ra}]_{\text{GW}}$  and the  $[^{223}\text{Ra}/^{228}\text{Ra}]_{\text{corr}}$ , like the  $[^{234}\text{U}/^{238}\text{U}]_{\text{GW}}$ , may be a robust approach to locating  $\text{U}_{\text{solid}}$  deposits.  $^{232}\text{Th}_{\text{solid}}$  and  $\text{U}_{\text{solid}}$  are co-deposited in igneous rocks, but over time, alteration events preferentially mobilize redox-sensitive U over insoluble Th. The  $[^{223}\text{Ra}/^{228}\text{Ra}]_{\text{corr}}$  reflects the degree of fractionation between their parent nuclides and so can be used to distinguish between localities where  $\text{U}_{\text{solid}}$  has been leached or deposited, which would

1 produce low and high ARs, respectively. At Forsmark/SFR, the  $[^{223}\text{Ra}/^{228}\text{Ra}]_{\text{corr}}$  should be lower in  
 2 groundwater that interacts with Ca-U(VI)-silicates than with  $\text{UO}_{2+x}$  because these minerals were  
 3 deposited in Th-rich pegmatites and Th-poor fractures, respectively. The  $[^{223}\text{Ra}/^{228}\text{Ra}]_{\text{corr}}$ , supplemented  
 4 by geochemical models and previous mineralogic characterization, may help to resolve the locations of  
 5  $\text{U}_{\text{solid}}$  leaching and deposition zones and to identify the sources of U(VI) (e.g. Precambrian or post-glacial  
 6 U(VI)-minerals) to be identified.

7 In theory, a curve of the  $[^{223}\text{Ra}/^{228}\text{Ra}]_{\text{corr}}$  and  $[\text{U}_{\text{aq}}]$  evolution along a redox front should be similar to that  
 8 of the  $[^{234}\text{U}/^{238}\text{U}]_{\text{GW}}$  curve from Osmond et al., (1983) because both ARs are low where uranium has been  
 9 dissolved and transported away from its origin and are high where secondary  $\text{U}_{\text{solids}}$  have accumulated  
 10 (e.g. Kumer et al., 2016).

11 The curve traced from the Forsmark data seems to show background, leaching, and deposition sectors  
 12 (Figure 10.b–c) similar to those of Osmond et al. (1983) but does not expose a redox front at repository  
 13 depth. If analogous to the Osmond & Cowart (1983) curve, the palaeoredox front should show a broad  
 14 range of  $[^{223}\text{Ra}/^{228}\text{Ra}]_{\text{corr}}$  together with high  $[\text{U}_{\text{aq}}]$ , which at Forsmark/SFR are the samples that have ARs  
 15 0.4 – 20 and  $> 10 \mu\text{gU/L}$  (Figure 10.c). However,  $[^{223}\text{Ra}/^{228}\text{Ra}]_{\text{corr}}$  ARs are most variable at ~200 m depth,  
 16 which is shallower than the 400 – 600 m depth of the  $[\text{U}_{\text{aq}}]$  anomaly.

17 Furthermore, ARs should be at a minimum in the “ $\text{U}_{\text{solid}}$  leaching” sector but instead scatter around the  
 18 site median (1 – 4 versus 2.9), which is within the range of the  $\text{U}_{\text{solid}}$ -rich pegmatites or the meta-granite  
 19 (Figure 10.c). Finally, the groundwater classifications do not show a logical relation to leaching or  
 20 deposition; leaching signatures are no more likely than deposition in glacial groundwaters and can prevail  
 21 in low redox, non-marine groundwater (e.g. KFM08A.2(550); Figure 10.c). Rather than a post-glacial  
 22 redox front, on-going dissolution of old Ca-U(VI)-minerals and precipitation  $\text{UO}_{2+x}$  may dictate  
 23 groundwater’s position along the curve. This interpretation is corroborated by results from the  
 24 mineralogic characterization and geochemical modelling studies. That is, the types and textures of  $\text{U}_{\text{solids}}$   
 25 near the groundwaters in the respective sectors are consistent with their classification as background,  
 26 leaching, or deposition (Table 4).

27 For instance, KFM01D.2(340) and KFM03A.1(970) are located in the bedrock domains where minimal  
 28 brittle deformation has occurred (Figure 2.b), which, like the nearby uraninite, shows no evidence of  
 29 hydrothermal alteration (Table 4). The low  $[^{223}\text{Ra}/^{228}\text{Ra}]_{\text{corr}}$  in these samples also suggest that the  $\text{U}_{\text{solid}}$   
 30 and  $\text{Th}_{\text{solid}}$  remain co-located and that the nearby uranium has not been mobilized even though these these  
 31 transition and non-marine groundwaters contain a glacial meltwater component (Figure 10.c).

Ca-U(VI)-silicates were exclusively found in pegmatites around the groundwaters that fall in the leaching sector (Table 4). Some of these minerals show recent Pb-loss in connection with alteration by carbonate-rich fluids, preserved as calcite. These alteration textures might be related to the bicarbonate in the brackish-marine and mixed groundwaters, which in this sector, can have high  $[U_{aq}]$  predominated by U(VI). Since the Ca-U(VI)-silicates were formed from the hydrothermal fluids that circulated in the brittle deformation zones, they are also present near the non-marine groundwater in KFM08A.2(550) (Figure 2.b). This and one transition groundwater (KFM11A.4(390)) have  $[^{223}\text{Ra}/^{228}\text{Ra}]_{\text{corr}}$  consistent with leaching, but the low  $[U_{aq}]$  may be related to the lack of marine component, absence of bicarbonate dissolution textures, and U(IV)<sub>aq</sub> predominance in these groundwaters. Although  $[^{223}\text{Ra}/^{228}\text{Ra}]_{\text{corr}}$  less than the background metagranite could be expected in the leaching sector, the AR is average and so may reflect groundwater interaction with U<sub>solid</sub>-rich pegmatites or uranium fractionation related to hydrothermal fluids (Figure 10.c).

Near the groundwaters in the deposition-sector UO<sub>2+x</sub> solids were observed (Figure 10.c; Table 4), which forward models suggested to represent an actively precipitating U(IV)<sub>solid</sub> rather than a U(VI)<sub>solid</sub> of glacial origin (Section 5.2.2). Likewise, speciation-solubility calculations produce relatively high U(IV)<sub>aq</sub> proportions and UO<sub>2.67</sub> saturation indexes for these groundwaters (Figure 3). Finally, non-steady state  $[^{224}\text{Ra}/^{228}\text{Ra}]_{\text{GW}}$  (>1.5) and  $[^{223}\text{Ra}/^{226}\text{Ra}]_{\text{GW}}$  (>0.046) were prevalent in the “deposition” sector, so these may groundwaters may be located at the boundary of two distinct groundwater mixtures (Section 4.3.2). Fluctuation of this boundary could allow U<sub>aq</sub>-rich groundwaters to occasionally ingress and deposit U<sub>solid</sub> after a minor decrease in pe-value and/or bicarbonate (Section 5.2.1).

Forsmark and SFR  $[^{223}\text{Ra}/^{228}\text{Ra}]_{\text{corr}}$  do follow a curve similar to that of the redox front generated by Osmond et al. (1983). Whether a groundwater falls into the background, leaching, or deposition sector, in addition to  $[^{223}\text{Ra}/^{228}\text{Ra}]_{\text{corr}}$  and  $[U_{aq}]$ , can be justified through the interaction of geologically-old U(VI) minerals (Krall et al. 2015, 2019) with the present groundwaters. This model better accounts for the variability in  $[U_{aq}]$  throughout the site (Section 2.2, 4.2) than does the oxidizing glacial meltwater model.

## 6 Conclusions

This study, prompted by the need to address an unusual distribution of U(VI)<sub>aq</sub> throughout the deep groundwaters at a proposed nuclear fuel repository, has reported the full Ra isotope quartet from anoxic groundwaters at depths up to 1000 m. Although the Ra<sub>GW</sub> of short-lived isotopes are rarely reported from crystalline rocks, the results could be interpreted in the context of the site background knowledge. This showed that Ra isotope systematics may be useful for assessing residence times and redox reactions in Holocene groundwater systems. A novel  $[^{223}\text{Ra}/^{226}\text{Ra}]_{\text{GW}}$  residence time model and PHREEQC speciation

calculations showed that iron, sulfur, and uranium redox systems were equally far from thermodynamic equilibrium in  $U_{aq}$ -containing groundwaters of ancient and modern marine origin. From this, it was inferred that local  $[U_{aq}]$  is governed by on-going water-rock interactions.

Interpretation of  $[^{223}Ra/^{228}Ra]_{corr}$ ,  $[U_{aq}]$ , mineralogic characterization, and forward geochemical modelling support the hypothesis that  $U_{aq}$  is related to geologically old Ca-U(VI)-silicate minerals. However, these results cannot rule out the possibility that Forsmark uranium was oxidized more recently, for instance by penetrating glacial meltwater.

To validate the  $Ra_{GW}$  residence time and redox front models presented here, more widespread application of short-lived  $^{223}Ra_{GW}$  and  $^{224}Ra_{GW}$  analyses in anoxic groundwaters would be helpful. Finally, the stabilization of  $U(VI)_{aq}$  in  $Ca_2UO_2CO_3^0$ -predominated groundwaters with pe-values as low as  $-4.5$  should be further assessed in the context of repository safety.

### Acknowledgements

The authors are grateful for the assistance of Cecilia Berg and Ignasi Puigdomenech at SKB, as well as for the comments from two anonymous reviewers that greatly improved the discussion. This study was supported by the Swedish Nuclear Fuel and Waste Management Company and the European Union Seventh Framework Programme for research, technological development and demonstration under Grant Agreement no. 290336.

## 1 Appendix 1:

2 The Forsmark and SFR data were plotted alongside the curves in Figure 7 in order to determine whether  
 3 similar ages can be derived from a particular set of non-steady state [ $^{224}\text{Ra}/^{228}\text{Ra}$ ] and [ $^{223}\text{Ra}/^{226}\text{Ra}$ ] ARs.  
 4 Without such visualization, the evolution of the two ARs as indicators of groundwater age is difficult to  
 5 comprehend, in that both involve several terms of exponential growth and decay. To further understand  
 6 the impact of variations in initial isotope activities and ARs, we wrote a Matlab code that generates  
 7 numerical solutions to the Bateman equations for four isotopes in a series.

8 As described in Section 5.1.2, it is straightforward to work with the equations for decay of a parent  
 9 isotope (Eqn A.1) and for the growth and decay of a daughter isotope (Eqn A.2)

### 10 Eqn A.1

$$11 \quad \frac{dN_1}{dt} = -\lambda_1 N_1 \rightarrow N_1 = N_{1,t=0} e^{-\lambda_1 t}$$

### 12 Eqn A.2

$$13 \quad \frac{dN_2}{dt} = -\lambda_2 N_2(t) + \lambda_1 N_1(t)$$

14 Where solution for  $N_1$  from Eqn. A.1 can be substituted into Eqn A.2, which can then be integrated and  
 15 solved in terms of  $N_2$  for a given point in time.

16 These substitutions are propagated through the equations for growth and decay of  $i$ th daughter isotope:

### 17 Eqn A.3

$$18 \quad \frac{dN_i(t)}{dt} = -\lambda_i N_i(t) + \lambda_{i-1} N_{i-1}(t),$$

19 but these equations become computationally intensive to solve beyond the first daughter nuclide.  
 20 Nevertheless, the matrix exponential method (see the lecture slides of Marc Spiegelman of Columbia  
 21 University, [http://www.ldeo.columbia.edu/~mspieg/e4300/CompletePDFs/Lecture14\\_complete.pdf](http://www.ldeo.columbia.edu/~mspieg/e4300/CompletePDFs/Lecture14_complete.pdf)) can  
 22 be used to solve the system of coupled, linear, first order differential equations in MatLab. For this  
 23 approach, the system is converted to:

### 24 Eqn A.4

$$25 \quad \frac{d\mathbf{N}(t)}{dt} = \mathbf{A}\mathbf{N}, \text{ with } \mathbf{N}(0) = \mathbf{N}_0$$

26

27 where  $\mathbf{N}$  is a vector that stores the results to the activity calculations and  $\mathbf{A}$  is a diagonal matrix of decay  
 28 constants:

$$29 \quad \mathbf{A} = \begin{pmatrix} -\lambda_1 & 0 & 0 & \dots & 0 \\ \lambda_2 & -\lambda_2 & 0 & \dots & 0 \\ 0 & \lambda_3 & -\lambda_3 & \dots & 0 \\ \vdots & \vdots & \vdots & \ddots & \vdots \\ 0 & 0 & 0 & \lambda_i & -\lambda_i \end{pmatrix}$$

The MatLab solver for ordinary differential equations (ode) was used to integrate the function expressed by Eqn A.4. Additional input parameters include a vector of initial activities ( $\underline{a}_0$ ) of length  $n$  (where  $n$  corresponds to the number of nuclides in a series for which to account), a vector of decay constants of length  $n$ , and a time range (e.g. 0 to 10,000 y).

At Forsmark, where U-series nuclides in the host rock are in secular equilibrium and decay of dissolved uranium contributes minor  $Ra_{GW}$  relative to that of U-series nuclides in the host rock, vectors for the initial activities of nuclides in each the  $^{238}U$ -,  $^{235}U$ -, and  $^{232}Th$ -series would be defined as follows:

$$\underline{a}_{0,238U} = [^{238}U \ ^{234}U \ ^{230}Th \ ^{226}Ra] = [1 \ 1 \ 1 \ 0]$$

$$\underline{a}_{0,235U} = [^{235}U \ ^{231}Pa \ ^{227}Th \ ^{223}Ra] = [0.046 \ 0.046 \ 0.046 \ 0]$$

$$\underline{a}_{0,232Th} = [^{232}Th \ ^{228}Ra \ ^{228}Th \ ^{224}Ra] = [1 \ 0 \ 1 \ 0]$$

However, in an aquifer that shows disequilibrium in U-series isotopes, that results in e.g.  $[^{230}Th/^{234}U]_{rk} \neq 1$  or  $[^{231}Pa/^{234}U]_{R+W} \neq 0.046$ , the initial parameters can be adjusted accordingly. Intermediate nuclides can be neglected if their half-lives are too short to influence the rate of arrival at steady state  $Ra_{GW}$  ARs.

For the  $^{232}Th$ -chain, the initial  $^{228}Ra_{GW}$  activity can be assumed to be zero, because the vector is configured to model the rate of Ra ingrowth into the water after alpha recoil from the Th parents.

Activities for individual Ra isotopes can be generated for a given number of time-steps, e.g. 100,000 points in time between  $t = 0$  and  $t = 10,000y$ . Unless the bulk activity of parents in the solid- and aqueous-phase are known, these activity vectors are meaningless unless converted to  $[^{224}Ra/^{228}Ra]$  and  $[^{223}Ra/^{226}Ra]$  activity ratios by dividing the vectors containing the  $^{224}Ra$  and  $^{223}Ra$  “activities” by those containing the  $^{228}Ra$  and  $^{226}Ra$  “activities.” The two AR vectors (which are indexed for equivalent time-steps) were plotted against each other to generate a curve that represents the locus of points where the  $[^{223}Ra/^{226}Ra]$  age equals the  $[^{224}Ra/^{228}Ra]$  age. The concept is similar to a Concordia curve for the U-Pb system.

The  $[^{223}Ra/^{226}Ra]$  vector generated in this Matlab model, shows good agreement with that generated by the simplified Equation 8 (Section 5.1.2). Therefore, accounting for ingrowth by parents higher than  $^{227}Th$  and  $^{230}Th$  will not change the ARs calculated for a given time,  $t$ , unless initial values for the radium progenitors in the  $\underline{a}_0$  vectors deviate from equilibrium.

To validate the model for the case of  $^{226}Ra_{w,t=0} \neq 0$  (Section 5.1.3), the response of  $[^{223}Ra/^{226}Ra]$  to a variations in  $^{226}Ra_{w,0}$  was tested. This is conceptually equivalent to a scenario of  $^{226}Ra_{GW}$  advection through variably U-enriched fractures. The sensitivity of  $^{223}Ra_{w,0}$  need not be tested because  $^{223}Ra_{GW}$  adapts and arrives at a steady state groundwater activity (represented in the model as 0.046) very soon after a groundwater enters a fracture that supports higher or lower  $Ra_{GW}$ . As compared to the original simulation, where  $^{226}Ra_{w,t=0} = 0$ , values of  $10^{-2}$ ,  $10^{-1}$ , and  $10^1$  were substituted for  $^{226}Ra_{w,t=0}$ . Since the progenitors parents in the  $\underline{a}_{0,238U}$  are set to 1 (or  $10^0$ ), the  $^{226}Ra_{w,t=0} = 10^{-2}$  and  $10^{-1}$  tests emulate a scenario wherein groundwater enters a fracture environment that supports  $^{226}Ra_{GW}$  activities that exceed that of the previous environments by factors of  $10^2$  and  $10^1$ , respectively. Conversely, the  $^{226}Ra_{w,0} = 10^1$  scenario simulates groundwater entering an environment that supports one order-of-magnitude lower  $Ra_{GW}$  than the previous environment. The results of these sensitivity tests and their implications for the validity of our model are discussed in Section 5.1.3.



## References

- Andrews, J. N., Ford, D. J., Hussain, N., Trivedi, D., & Youngman, M. J. (1989). Natural radioelement solution by circulating groundwaters in the Stripa granite. *Geochimica et Cosmochimica Acta*, 53(8), 1791-1802.
- Asikainen, M., & Kahlos, H. (1979). Anomalously high concentrations of uranium, radium and radon in water from drilled wells in the Helsinki region. *Geochimica et Cosmochimica Acta*, 43(10), 1681-1686.
- Asikainen, M. (1981). Radium content and the  $^{226}\text{Ra}/^{228}\text{Ra}$  activity ratio in groundwater from bedrock. *Geochimica et Cosmochimica Acta*, 45(8), 1375-1381.
- Auqué, L., Gimeno, M. J., Gómez, J., & Nilsson, A. C. (2008). Potentiometrically measured Eh in groundwaters from the Scandinavian Shield. *Applied Geochemistry*, 23(7), 1820-1833.
- Belli, K. M., DiChristina, T. J., Van Cappellen, P., & Taillefert, M. (2015). Effects of aqueous uranyl speciation on the kinetics of microbial uranium reduction. *Geochimica et Cosmochimica Acta*, 157, 109-124.
- Charette, M.A., Buesseler, K.O., Andrews, J.E. (2001). Utility of radium isotopes for evaluating the input and transport of groundwater-derived nitrogen to a Cape Cod estuary. *Limnol. Oceanogr.* 46, 465–470.
- Cuney, M., & Friedrich, M. (1987). Physicochemical and crystal-chemical controls on accessory mineral paragenesis in granitoids: implications for uranium metallogenesis. *Bulletin de mineralogie*, 110(2-3), 235-247.
- Cowart, J. B. (1980). The relationship of uranium isotopes to oxidation/reduction in the Edwards carbonate aquifer of Texas. *Earth and Planetary Science Letters*, 48(2), 277-283.
- Davidson, M. R., and B. L. Dickson. (1986). A porous flow model for steady-state transport of radium in ground waters. *Water Resources Research*, 22, 34–44.
- Drake, H., Tulborg, E-L. and MacKenzie, A. B. (2009). Detecting the near-surface redox front in crystalline bedrock using fracture mineral distribution, geochemistry and U-series disequilibrium. *Applied Geochemistry*, 24, 1023-1039.
- Ewing, R. C., Haaker, R. F., & Lutze, W. (1981). Leachability of zircon as a function of alpha dose. *MRS Online Proceedings Library Archive*, 11.
- Fleischer, R. L., and R. O. Raabe. (1978). Recoiling alpha-emitting nuclei: Mechanisms for uranium-series disequilibrium. *Geochimica et Cosmochimica Acta*, 42, 973–978.
- Fox, P.M., Davis, J.A., Zachara, J.M. (2006). The effect of calcium on aqueous uranium(VI) speciation and adsorption to ferrihydrite and quartz. *Geochim. Cosmochim. Acta* 70, 1379–1387.
- Garcia-Solsona E., Garcia-Orellana, J., Masque, P., Dulaiova, H. (2008). Uncertainties associated with  $^{223}\text{Ra}$  and  $^{224}\text{Ra}$  measurements in water via a Delayed Coincidence Counter (RaDeCC), *Marine Chemistry*, 109(3–4), pp. 198–219.
- Gascoyne, M. (2004). Hydrogeochemistry, groundwater ages and sources of salts in a granitic batholith on the Canadian Shield, southeastern Manitoba. *Applied Geochemistry* 19:519–560.
- Giblin, A. M., & Appleyard, E. C. (1987). Uranium mobility in non-oxidizing brines: field and experimental evidence. *Applied geochemistry*, 2(3), 285-295.
- Giffaut, E., Grive, M., Blanc, Ph., Vieillard, Ph., Colas, E., Gailhanou, H., Gaboreau, S., Marty, M., Made, B., and Duro, L. (2014). *Applied Geochemistry*, 49, 225-236.

- 1 Giffaut, E., Grivé, M., Blanc, Ph., Vieillard, Ph., Colàs, E., Gailhanou, H., Gaboreau, S., Marty, N., Madé, B. and  
2 Duro, L. (2014). Andra thermodynamic database for performance assessment: ThermoChimie. *Applied*  
3 *Geochemistry*, 49, 225–236.
- 4 Gimeno, M., Auqué, L., Gómez, J. (2006). Appendix C: Chemnet's issue report, Forsmark area version 2.1. In: SKB  
5 Hydrogeochemical evaluation of the Forsmark site, modelling stage 2.1 – issue report. SKB R-06-09,  
6 Svensk Kärnbränslehantering AB, 153-187.
- 7 Gimeno, M.J., Auqué, L.F., Gómez, J. (2007). PHREEQC Modelling. Appendix 3. SKB Report R-06-70. SKB,  
8 Stockholm, Sweden.
- 9 Gimeno, M.J., Auqué, L.F., Gómez, J.B., Acero, P. (2008). Water–rock interaction modelling and uncertainties of  
10 Mixing Modelling. SDM-Site Forsmark. SKB Report R-08-86. SKB, Stockholm, Sweden.
- 11 Grolander, S. (2009). Radon as a groundwater tracer in Forsmark and Laxemar. SKB report R-09-47, SKB,  
12 Stockholm, Sweden.
- 13 Hallbeck, L., & Pedersen, K. (2012). Culture-dependent comparison of microbial diversity in deep granitic  
14 groundwater from two sites considered for a Swedish final repository of spent nuclear fuel. *FEMS*  
15 *microbiology ecology*, 81(1), 66-77.
- 16 Hemingway, B. S. (1982). *Thermodynamic properties of selected uranium compounds and aqueous species at*  
17 *298.15 K and 1 bar and at higher temperatures; preliminary models for the origin of coffinite deposits* (No.  
18 82-619). US Geological Survey.
- 19 Hermansson, T., Stephens, M.B., Corfu, F., Page, L., Andersson, J. (2007). Penetrative ductile deformation and  
20 amphibolites-facies metamorphism prior to 1851 Ma in the western part of the Svecofennian orogen,  
21 Fennoscandian Shield. *Precambrian Res.* 153, 29–45.
- 22 Hermansson, T., Stephens, M.B., Corfu, F., Page, L.M., Andersson, J. (2008). Migratory tectonic switching, western  
23 Svecofennian orogen, central Sweden: constraints from U/Pb zircon and titanite geochronology.  
24 *Precambrian Res.* 161, 250–278.
- 25 Kamyshny, A. Jr., Zilberbrand, M., Ekelchik, I., Voitkovski, T., Gun, J. and Lev, O. (2008). Speciation of  
26 polysulphides and zerovalent sulfur in sulphide-rich water wells in southern and central Israel. *Aquatic*  
27 *Geochemistry* vol. 14, 171-192.
- 28 Kigoshi, K. (1971). Alpha recoil  $^{234}\text{Th}$ : Dissolution in water and the  $^{234}\text{U}/^{238}\text{U}$  disequilibrium in nature. *Science*, 173,  
29 47–48.
- 30 Krall, L., Sandström, B., Tullborg, E.-L., & Evins, L.Z. (2015). Natural uranium in Forsmark, Sweden: The solid  
31 phase. *Applied Geochemistry*, 59, pp 178-188.
- 32 Krall, L., Trezzi, G., Garcia-Orellana, J., Rodellas, V., Mörtz, C. M., & Andersson, P. (2017). Submarine  
33 groundwater discharge at Forsmark, Gulf of Bothnia, provided by Ra isotopes. *Marine Chemistry*, 196,  
34 162-172.
- 35 Krall, L., Evins, L. Z., Kooijman, E., Whitehouse, M., & Tullborg, E. L. (2019). Tracing the palaeoredox conditions  
36 at Forsmark, Sweden, using uranium mineral geochronology. *Chemical Geology*, 506, 68-78.
- 37 Krishnaswami, S., W. C. Graustein, K. K. Turekian, and J. F. Dowd (1982), Radium, thorium and radioactive lead  
38 isotopes in groundwaters: Application to the *in situ* determination of adsorption-desorption rate constants  
39 and retardation factors, *Water Resour. Res.*, 18(6), 1663–1675, doi:[10.1029/WR018i006p01663](https://doi.org/10.1029/WR018i006p01663).

- 1 Krishnaswami, S., Cochran, K. (2008). Appendix B Systematics of Radioactive Decay, *Radioactivity in the*  
2 *Environment*, Volume 13, 2008, Pages 425-431, ISSN 1569-4860, [http://dx.doi.org/10.1016/S1569-](http://dx.doi.org/10.1016/S1569-4860(07)00016-2)  
3 [4860\(07\)00016-2](http://dx.doi.org/10.1016/S1569-4860(07)00016-2).
- 4 Kumar, A., Karpe, R. K., Rout, S., Gautam, Y. P., Mishra, M. K., Ravi, P. M., & Tripathi, R. M. (2016). Activity  
5 ratios of  $^{234}\text{U}/^{238}\text{U}$  and  $^{226}\text{Ra}/^{228}\text{Ra}$  for transport mechanisms of elevated uranium in alluvial aquifers  
6 of groundwater in south-western (SW) Punjab, India. *Journal of environmental radioactivity*, 151, 311-320.
- 7 Laaksoharju, M., Smellie, J., Tullborg, E.-L. (2008). Bedrock hydrogeochemistry Forsmark, site descriptive  
8 modelling Forsmark. SKB R-08-47, Svensk Kärnbränslehantering AB.
- 9 MacKenzie, A.B., Scott, R.D., Linsalata, P., Miekeley, N. (1992). Natural decay series studies of the redox front  
10 system in the Pocos de Caldas uranium mineralization. *J. Geochem. Explor.*, 17, pp. 289– 322.
- 11 Martin, P., & Akber, R. A. (1999). Radium isotopes as indicators of adsorption–desorption interactions and barite  
12 formation in groundwater. *Journal of Environmental Radioactivity*, 46(3), 271-286.
- 13 Moore, W. S., Astwood, H. and Lindstrom, C. (1995). Radium isotopes in coastal waters on the Amazon shelf.  
14 *Geochim. Cosmochim. Acta* 59: 4285-4298.
- 15 Moore, W.S., Arnold, R. (1996). Measurement of  $^{223}\text{Ra}$  and  $^{224}\text{Ra}$  in coastal waters using a delayed coincidence  
16 counter. *J. Geophys. Res. C Ocean* 101, 1321–1329.
- 17 Moore, W.S., Reid, D.F. (1973). Extraction of radium from natural waters using manganese impregnated acrylic  
18 fibers. *J. Geophys. Res.* 78, 8880–8886. <http://dx.doi.org/10.1029/JC078i036p08880>.
- 19 Nilsson, A-C, Tullborg, E-L, Smellie, J., Gimeno, M., Gómez, J., Auqué, L., Sandström, B., Pedersen, K. (2011).  
20 SFR site investigation: Bedrock hydrogeochemistry. SKB R-11-06. Svensk Kärnbränslehantering AB.
- 21 Osmond, J. K., Cowart, J. B., & Ivanovich, M. (1983). Uranium isotopic disequilibrium in ground water as an  
22 indicator of anomalies. *The International Journal of Applied Radiation and Isotopes*, 34(1), 283-308.
- 23 Osmond JK, Cowart JB (1992) Ground water. In *Uranium-series disequilibrium*. Ivanovich M, Harmon RS (eds).  
24 Clarendon Press Oxford, p290-334
- 25 Parkurst, D.L. and Appelo, C.A.J. (2013). Description of input and examples for PHREEQC, Version 3. Chapter 43  
26 of Section A, Groundwater Book 6, Modeling Techniques. Techniques and Methods 6–A43. U.S.  
27 Geological Survey.
- 28 Porcelli, D. (2008). Investigating groundwater processes using U- and Th- series nuclides. In: Krishnaswami S,  
29 Cochran JK (eds) *U-Th series nuclides in aquatic systems*, Elsevier, London, 105-154.
- 30 Porcelli, D., & Swarzenski, P. W. (2003). The behavior of U-and Th-series nuclides in groundwater. *Reviews in*  
31 *Mineralogy and Geochemistry*, 52(1), 317-361.
- 32 Prikryl, J. D. (2008). Uranophane dissolution and growth in  $\text{CaCl}_2\text{--SiO}_2$  (aq) test solutions. *Geochimica et*  
33 *Cosmochimica Acta*, 72(18), 4508-4520.
- 34 Rodellas, V., Garcia-Orellana, J., Masqué, P., Font-Muñoz, J.S. (2015). The influence of sediment sources on  
35 radium-derived estimates of Submarine Groundwater Discharge. *Marine Chemistry* 171, 107-117.
- 36 Rößler, D. (2006). Reconstruction of the Littorina transgression in the Western Baltic Sea. Institut für Meereskunde  
37 Warnemünde.
- 38 Sandström, B., Tullborg, E.-L., Smellie, J., MacKenzie, A., Suksi, J. (2008). Fracture mineralogy of the Forsmark  
39 site. SKB R-Report R-08-102. SKB, Stockholm, Sweden.

- 1 Sandström, B., Tullborg, E. L., Larson, S. Å., & Page, L. (2009). Brittle tectonothermal evolution in the Forsmark  
2 area, central Fennoscandian Shield, recorded by paragenesis, orientation and  $^{40}\text{Ar}/^{39}\text{Ar}$  geochronology of  
3 fracture minerals. *Tectonophysics*, 478(3-4), 158-174.
- 4 Sandström, B., Nilsson, K., Tullborg, E.-L. (2011). Fracture Mineralogy Including Identification of Uranium Phases  
5 and Hydrogeochemical Characterisation of Groundwater in Borehole KFR106. SKB P-Report P-11-41.  
6 SKB, Stockholm, Sweden.
- 7 Sandström, B., Tullborg, E.-L. (2011). Fracture mineralogy and geochemistry of borehole sections sampled for  
8 groundwater Chemistry and Eh. SKB P-Report P-11-01. SKB, Stockholm, Sweden.
- 9 Sheng, L., Szymanowski, J., & Fein, J. B. (2011). The effects of uranium speciation on the rate of U (VI) reduction  
10 by *Shewanella oneidensis* MR-1. *Geochimica et Cosmochimica Acta*, 75(12), 3558-3567.
- 11 Sheng L. and Fein J. B. (2014) Uranium reduction by *Shewanella oneidensis* MR-1 as a function of  $\text{NaHCO}_3$   
12 concentration: Surface complexation control of reduction kinetics. *Environ. Sci. Technol.* **48**, 3768–3775.
- 13 Shvareva, T. Y., Mazeina, L., Gorman-Lewis, D., Burns, P. C., Szymanowski, J. E., Fein, J. B., & Navrotsky, A.  
14 (2011). Thermodynamic characterization of boltwoodite and uranophane: Enthalpy of formation and  
15 aqueous solubility. *Geochimica et Cosmochimica Acta*, 75(18), 5269-5282.
- 16 Singer, D.M., Maher, K., Brown, G.E. (2009). Uranyl-chlorite sorption/desorption: evaluation of different U(VI)  
17 sequestration processes. *Geochim Cosmochim Acta* 73:5989–6007
- 18 Smellie, J., Tullborg, E.-L., Nilsson, A.-C., Sandström, B., Waber, N., Gimeno, M., Gascoyne, M. (2008).  
19 Explorative Analysis of Major Components and Isotopes. SKB R-Report R-08-84. SKB, Stockholm,  
20 Sweden.
- 21 Stephens, M.B., Lundqvist, S., Bergman, T., Ekström, M. (2005). Forsmark site investigation. Bedrock Mapping.  
22 Petrographic and Geochemical Characteristics of Rock Types Based on Stage 1 (2002) and Stage 2 (2003)  
23 Surface Data. SKB P-Report P-04-08. SKB, Stockholm, Sweden.
- 24 Stewart, B. D., Amos, R. T., Nico, P. S., & Fendorf, S. (2011). Influence of Uranyl Speciation and Iron Oxides on  
25 Uranium Biogeochemical Redox Reactions. *Geomicrobiology Journal*, 28(5/6), 444-456.  
26 doi:10.1080/01490451.2010.507646
- 27 Stookey, L. (1970). Ferrozine - A new spectrophotometric reagent for iron. *Analytical Chemistry*, 42, 779–781.
- 28 Suksi, J., Rasilainen, K., Pitkänen, P. (2006). Variations in the  $^{234}\text{U}/^{238}\text{U}$  activity ratio in groundwater—a key to  
29 characterise flow system? *Phys. Chem. Earth* 31, 556–571.
- 30 Suksi, J., Salminen, S. (2007). Study of U oxidation states in groundwater with high U concentrations. SKB P-07-  
31 54, Svensk Kärnbränslehantering AB.
- 32 Sun, Y., Torgersen, T. (1998). The effects of water content and Mn-fiber surface conditions on measurement by  
33 emanation. *Mar. Chem.* 62, 299–306. [http://dx.doi.org/10.1016/S0304-4203\(98\)00019-X](http://dx.doi.org/10.1016/S0304-4203(98)00019-X).
- 34 Taylor, S. D., Marcano, M. C., Rosso, K. M., & Becker, U. (2015). An experimental and ab initio study on the  
35 abiotic reduction of uranyl by ferrous iron. *Geochimica et Cosmochimica Acta*, 156, 154-172.
- 36 Thoenen, T., Hummel, W., Berner, U., and Curti, E. (2014). The PSI/Nagra Chemical Thermodynamic Database  
37 12/07. Paul Scherrer Institut, PSI Bericht Nr. 14-04. freely available for the PHREEQC format at  
38 <https://www.psi.ch/les/database>.

- 1 Tomita, J., Satake, H., Fukuyama, T., Sasaki, K., Sakaguchi, A., & Yamamoto, M. (2010). Radium geochemistry in  
2 Na–Cl type groundwater in Niigata Prefecture, Japan. *Journal of environmental radioactivity*, 101(3), 201-  
3 210.
- 4 Tomita, J., Zhang, J., & Yamamoto, M. (2014). Radium isotopes ( $^{226}\text{Ra}$  and  $^{228}\text{Ra}$ ) in Na–Cl type groundwaters from  
5 Tohoku District (Aomori, Akita and Yamagata Prefectures) in Japan. *Journal of Environmental*  
6 *Radioactivity*, 137, 204-212.
- 7 Tricca, A., Porcelli, D., and Wasserburg, G. J. (2000). Factors controlling the ground water transport of U, Th, Ra,  
8 and Rn. *Proceedings of the Indian Academy of Sciences*, 109, 95–108.
- 9 Tullborg, E. L., Smellie, J., Nilsson, A. C., Gimeno, M. J., Auqué, L. F., Bruchert, V., & Molinero, J. (2010). *SR-*  
10 *Site-sulphide content in the groundwater at Forsmark* (No. SKB-TR--10-39). Swedish Nuclear Fuel and  
11 Waste management Co.
- 12 Tullborg, E. L., Suksi, J., Geipel, G., Krall, L., Auqué, L., Gimeno, M., & Puigdomenech, I. (2017). The  
13 occurrences of  $\text{Ca}_2\text{UO}_2(\text{CO}_3)_3$  complex in Fe (II) containing deep groundwater at Forsmark, eastern  
14 Sweden. *Procedia Earth and Planetary Science*, 17, 440-443. Vengosh, A., Hirschfeld, D., Vinson, D.,  
15 Dwyer, G., Raanan, H., Rimawi, O., ... & Zaarur, S. (2009). High naturally occurring radioactivity in fossil  
16 groundwater from the Middle East. *Environmental science & technology*, 43(6), 1769-1775.
- 17 Vinson, D.S., Vengosh, A., Hirschfeld, D., and Dwyer, G.S. (2009). Relationships between radium and radon  
18 occurrence and hydrochemistry in fresh groundwater from fractured crystalline rocks, North Carolina  
19 (USA). *Chemical Geology*, v. 260, p. 159-171.

**Table 1:** Geochemical analyses selected from SICADA, alongside the calculated total dissolved solids (TDS) and the pe values calculated from the Fe(II)/Fe(III) and S(-II)/S(VI) couples with PHREEQC and the Nagra database. Content in bold shows where data was obtained from a different analyses of the same borehole section in the monitoring data.

Borehole section	DPT (m)	Type	T °C	pH	Na	K	Ca	Mg	HCO <sub>3</sub> <sup>-</sup>	Cl	SO <sub>4</sub> <sup>2-</sup>	HS <sup>-</sup> mg/L	Br	F	Si	Fe(II)	Mn(II)	Li	Sr	U µg/L	Ba µg/L	TDS g/L	pe Fe	pe S
KFR106.2	187	M	13	7.4	1800	15	760	180	110	4200	330	--	14	1.3	5.3	1.4	1.2	0.050	9.3	31	--	7.5	-4.5	--
KFM02A.3	495	BM	8.2	7.4	2100	35	980	230	130	5600	460	0.15	18	1.5	7.1	2.5	2.1	0.045	7.7	150	94	9.6	-4.7	-3.8
KFR02.1	239	M	11	7.4	1500	7.1	1200	160	85	4600	400	<b>0.01</b>	17	1.4	5.4	1.3	1.5	0.066	16	15	120	8.0	-4.5	-3.7
KFR02.2	213	M	10	7.6	1500	7.2	1200	150	81	4500	340	<b>0.02</b>	16	1.3	6.1	1.6	1.3	0.059	17	12	160	7.9	-5.1	-3.9
KFR02.3	185	M	10	7.7	1400	6.9	1200	140	77	4500	330	<b>0.02</b>	17	1.3	6.2	1.0	1.0	0.072	17	14	140	7.7	-5.1	-4.0
KFR02.4	147	G	11	7.8	1200	5.2	1000	93	56	3700	170	0.02	15	1.2	5.9	0.40	0.52	0.064	15	17	130	6.3	-5.0	-4.1
KFM11A.4	390	T	9.2	7.7	1400	6.1	1400	30	10	4400	240	<b>0.39</b>	31	1.1	5.3	0.25	0.14	0.051	19	0.39	88	7.6	-4.7	-4.3
KFR102A.5	195	M	<b>13</b>	<b>7.7</b>	1800	9.5	770	120	110	4200	360	<b>0.01</b>	19	1.5	6.1	0.77	0.70	0.053	12	6.4	130	7.4	-5.2	-4.0
KFR106.1	261	G	11	7.7	1100	14	490	77	110	2500	170	--	10	1.4	5	0.60	0.44	0.040	6.7	30	--	4.5	-5.0	--
KFM03A.4	631	T	6.6	7.6	1700	17	1500	63	23	5800	200	0.16	35	2.1	7.4	0.66	0.41	0.030	16	39	170	9.5	-4.6	-4.1
KFM02A.5	418	BM	7.2	7.6	1800	21	1200	200	100	5500	410	0.32	23	1.3	8.4	0.58	1.9	2.4	11	38	110	9.4	-4.4	-4.0
KFM02B.4	407	BM	8.9	<b>7.5</b>	2100	29	1100	220	110	5500	480	0.09	24	1.7	9.9	2.5	2.3	0.14	10	23	140	9.8	-4.9	-3.9
KFM02B.2	484	BM	9.3	<b>7.4</b>	2300	39	970	240	130	5500	510	0.04	23	1.7	9.3	4.2	2.2	0.057	8.1	9.4	120	9.8	-4.7	-3.7
KFM08A.2	551	NM	7.5	8.8	1500	11	2000	15	14	6300	100	0.02	49	1.3	5.2	0.30	0.16	0.021	21	0.74	360	10	-7.7	-5.3
KFR102A.2	389	M	<b>10</b>	<b>7.5</b>	1500	12	660	110	91	3500	290	0.03	17	1.4	6.5	0.95	0.74	0.047	9.8	21	110	6.3	-4.6	-3.8
KFR 101.1	240	G	6.3	7.8	740	5.8	370	31	68	1900	40	0.07	10	1.6	5.2	0.27	0.45	0.029	5.6	57	560	3.2	-5.0	-4.4
KFR 105.5	117	M	<b>6</b>	<b>7.6</b>	1300	6.3	820	110	93	3600	300	<b>0.01</b>	18	1.1	6.1	0.74	0.54	0.058	11	27	82	6.3	-4.7	-3.9
KFR 105.1	154	G	<b>8.9</b>	<b>7.7</b>	1300	6.7	680	96	85	3200	240	<b>0.01</b>	16	1.3	5.8	0.72	1.5	0.065	12	32	160	5.7	-5.0	-4.0
KFM 11A.2	594	T	<b>8.5</b>	<b>7.8</b>	1700	15	1400	78	64	5400	200	0.04	34	1.0	6.2	3.0	0.59	0.044	18	3.3	170	9.0	-5.9	-4.2
KFM 03A.1	969	NM	<b>8.2</b>	<b>7.7</b>	2200	10	4000	10	15	11000	40	1.2	99	1.5	6.8	0.99	0.09	0.032	48	0.45	1100	17	-4.4	-4.9
KFM 01D.2	343	T	11	7.6	1400	11	1300	34	40	4600	100	3.9	28	1.3	14.7	0.12	0.19	0.031	13	0.86	620	7.6	-4.1	-4.3
KFR01	134	M	8.7	7.6	1400	8.8	610	130	110	3400	370	<b>0.01</b>	11	1.1	5.3	0.44	0.76	0.060	8.2	2.8	55	6.1	-4.5	-3.9
KFR07A	94	BM	<b>11</b>	<b>7.4</b>	1400	14	590	160	110	3700	410	<b>0.01</b>	13	1.5	5.8	2.6	1.5	0.049	6.9	8.2	36	6.4	-4.9	-3.7

**M** Mixed brackish marine (SFR)  
**BM** Brackish marine (Littorina-Glacial)  
**G** Brackish glacial  
**T** Transition (non-marine brackish with some Littorina)  
**NM** Brackish to saline non-marine

**Table 2:** Bulk activities and activity ratios for U- and Th-series isotopes in Forsmark groundwaters, alongside depth of the borehole section. The unit “dpm” refers to disintegrations per minute.

Borehole section	<sup>238</sup> U <sup>1</sup>	<sup>234</sup> U <sup>1</sup>	<sup>226</sup> Ra <sup>1</sup>	<sup>226</sup> Ra	σ	<sup>222</sup> Rn <sup>1</sup>	σ <sup>1</sup>	<sup>223</sup> Ra	σ	<sup>228</sup> Ra	σ	<sup>224</sup> Ra	σ	$\frac{^{223}\text{Ra}}{^{226}\text{Ra}}$	σ	$\frac{^{224}\text{Ra}}{^{228}\text{Ra}}$	σ	$\frac{^{223}\text{Ra}_{\text{corr}}}{^{228}\text{Ra}}$	σ
	dpm/L		dpm/L			·10 <sup>3</sup> dpm/L		dpm/L				dpm/L							
KFR106.2(190)	23	67	--	82	3.5	--	--	1.7	0.20	45	2.0	5.6	4.2	0.021	0.0026	0.12	0.094	0.28	0.034
KFM02A.3(500)	110	220	220	130	6.6	94	6.7	7.7	0.51	57	3.7	51	4.9	0.061	0.0052	0.89	0.10	2.9	0.28
KFR02.1(240)	9.8	35	--	85	5.8	--	--	3.9	0.35	81	5.6	63	5.3	0.046	0.0052	0.78	0.085	1.0	0.12
KFR02.2(210)	8.2	33	300	150	8.1	250	18	110	8.8	120	6.6	--	--	0.71	0.068			20	2.0
KFR02.3(190)	9.7	39	300	220	11	170	12	30	1.8	230	12	--	--	0.14	0.011			2.9	0.23
KFR02.4(150)	11	56	360	290	12	320	22	59	4.6	110	4.5	--	--	0.21	0.018			12	1.0
KFM11A.4(390)	0.29	0.75	68	150	10	31	0.60	20	1.9	150	11	100	11	0.13	0.015	0.69	0.093	2.9	0.36
KFR102A.5(200)	0.46	17	120	160	6.6	87	1.9	17	1.2	96	4.3	50	6.3	0.10	0.0084	0.52	0.070	3.9	0.31
KFR106.1(260)	21	45	--	71	3.0	--	--	2.3	0.24	76	3.4	18	6.2	0.032	0.0037	0.24	0.82	0.65	0.074
KFM03A.4(630)	26	40	1100	950	69	620	44	91	8.1	32	3.1	300	33	0.10	0.011	9.4	1.4	6.6	0.59
KFM02A.5(420)	21	75	250	110	7.4	53	3.8	15	1.6	300	19	240	20	0.13	0.017	0.80	0.086	1.1	0.14
KFM02B.4(410)	18	89	89	240	16	140	3.0	27	2.6	190	15	150	17	0.11	0.013	0.80	0.11	3.1	0.39
KFM02B.2(480)	6.6	18	92	120	8.1	39	0.90	7.8	0.84	150	11	25	5.7	0.062	0.0078	0.17	0.040	1.1	0.14
KFM08A.2(550)	0.55	1.1	320	260	10	27	1.9	19	1.7	91	5.4	120	14	0.073	0.0070	1.3	0.17	3.5	0.30
KFR 102A.2(390)	15	38	65	120	6.6	27	0.38	34	2.4	180	11	71	7.7	0.28	0.025	0.41	0.051	4.2	0.40
KFR 101.1(240)	45	150	180	270	15	14	0.30	11	0.95	170	10	81	7.1	0.039	0.004	0.47	0.050	1.3	0.15
KFR 105.5(120)	21	110	170	140	4.0	270	34	87	5.7	48	2.6	190	9.4	0.64	0.046	3.9	0.29	10	0.67
KFR 105.1(150)	26	120	360	330	8.8	210	6.4	79	6.3	100	4.0	170	16	0.24	0.020	1.7	0.17	10	0.84
KFM 11A.2(600)	2.5	5.9	260	600	31	32	0.96	21	2.0	570	32	430	28	0.035	0.0038	0.74	0.065	0.81	0.089
KFM 03A.1(970)	0.41	0.84	490	650	33	1.5	0.054	31	2.6	1700	9.0	1200	88	0.048	0.0047	0.69	0.062	0.38	0.038
KFM 01D.2(340)	0.60	1.8	250	880	45	58	4.1	37	3.8	1400	79	720	77	0.043	0.0049	0.52	0.063	0.58	0.068
KFR 07A <sup>2</sup> (130)	35	150	56	17	0.37	70	5.0	2.9	0.18	22	0.54	7.2	1.9	0.17	0.011	0.33	0.088	2.9	0.19
KFR 01 <sup>2</sup> (90)	12	62	50	31	0.70	42	0.66	3.6	0.20	72	2.0	26	14	0.12	0.0070	0.36	0.19	1.1	0.067

<sup>1</sup>Data obtained from SKB SICADA database

<sup>2</sup>Data reported in Krall et al. (2017)

**Table 3:** Definition of terms and variables in Equation 1, alongside a summary of the assumptions and mathematical operations that were made to arrive at Equation 8.

Term	Definition of variables	Meaning of term	Assumption / operation
$\frac{di_w}{dt}$	$di_w$ : Change in molar aqueous concentration of nuclide $i$ $dt$ : Change in time	Temporal evolution of concentration of nuclide $i$ in groundwater	Integrate to solve first-order differential equation for $i_w$
$v\left(\frac{di_w}{dx}\right)$	$v$ : Groundwater flow velocity $dx$ : Change in position $x$ along flow line	Advective input of $i$ to location $x$	Neglect term; rapid decay of short-lived nuclides inhibits advection
$bw_i i_R$	$b$ : Mass ratio of rock to water $w_i$ : Weathering rate of $i$ $i_R$ : Host rock concentration of $i$	Input of $i$ to water through weathering of $i$ -bearing minerals in host rock	Neglect term if half-life of $i$ is short relative to dissolution rate, so $i$ decays before dissolved by water
$b\epsilon_i \lambda_P P_R$	$\epsilon_i$ : Recoil release fraction for $i$ $\lambda_P$ : Decay constant for parent $P$ of $i$ $P_R$ : Host rock concentration of $P$	Input of $i$ to water through recoil from decay of mineralized parents	
$f_i \lambda_P P_{ads}$	$f_i$ : Fraction of $i$ recoiled into water after decay of adsorbed parents $P_{ads}$ : Adsorbed concentration of parent per mass rock	Input of $i$ to water after decay of adsorbed parents	Simplify to: $\lambda_P P_{R+W} = \lambda_P (b\epsilon_i P_R + f_i P_{ads} + P_w)$
$\lambda_P P_w$	$P_w$ : Groundwater $P$ concentration	Input of $i$ to water through decay of dissolved parents	
$\lambda_P P_{R+W}$	$P_{R+W}$ : Total concentration of parents in aquifer water and rock	Input of $i$ through decay of all parents in fracture	
$Q_i i_w$	$Q_i$ : Rate constant for $i$ precipitation $i_w$ : Groundwater concentration of $i$	Removal of $i$ from water through precipitation	Neglect term if half-life is short relative to rate of precipitation, so $i$ decays before precipitating
$\lambda_i i_w$	$\lambda_i$ : Decay constant for nuclide $i$ $i_w$ : Water concentration of $i$		Simplify to $-\lambda_i i_w(1 + K_i) = -\lambda_i i_w - \lambda_i i_{ads}$ to limit the number of variables in the exponent of Eqn 4. Then, substituting $K_i i_w$ for $i_{ads}$ in Eqn 4 so that $1 + K_i$ can be factored out of Eqn 5 and eliminated in Eqn 7, assuming $K_{223Ra} \sim K_{224Ra} \sim K_{226Ra} \sim K_{228Ra} = K_{Ra}$
$(1 + K_i); K_i = \frac{i_{ads}}{i_w}$	$K_i$ : Partition coefficient between dissolved and adsorbed atoms $i_{ads}$ : Adsorbed concentration of nuclide $i$ per mass of rock	Removal of $i$ from water through decay and adsorption	

**Table 4:** Summary of water-rock interaction indicators, matching groundwater geochemistry and radium ARs to solid phase observations collected by Krall et al. (2015, 2019), where possible.

Sector/sample (depth in meters)	GW-type	[U <sub>aq</sub> ] (µg/L)	U(IV) (%)	[ <sup>224</sup> Ra/ <sup>228</sup> Ra] <sub>GW</sub> AR			[ <sup>223</sup> Ra/ <sup>226</sup> Ra] <sub>GW</sub> AR			Petrographic description		
Background										Borehole (depth)	U mineral (Age, Ma)	Calcite
KFM03A.1(970)	Non-mar.	0.4	91	0.69	±	0.062	0.048	±	0.0047			
KFM01D.2 (340)	Trans.	0.9	87	0.52	±	0.063	0.043	±	0.0049	KFM01D(480)	Uraninite (1800)	
Leaching												
KFM11A.2(590)	Trans.	3.3	25	0.74	±	0.065	0.035	±	0.0038			
KFM11A.4(390)	Trans.	0.4	97	0.69	±	0.093	0.13	±	0.015			
KFM08A.2(550)	Non-mar.	3.5	93	1.3	±	0.17	0.073	±	0.007	KFM08D(550)	Uranothorite Ca-U(VI)-silicate UO <sub>2+x</sub>	
KFR01(90)	Mixed	2.8	15	0.78	±	0.085	0.012	±	0.007			
KFR07A(134)	BM	8.2	17	0.33	±	0.088	0.17	±	0.011			
KFR102A.2(390)	Mixed	21	28	0.41	±	0.051	0.28	±	0.025	KFR102A(450)	Uranothorite Ca-U(VI)-silicate	X
KFR102A.5(200)	Mixed	6.4	12	0.52	±	0.07	0.1	±	0.0084	KFR102A(200)	Uranothorite Ca-U(VI)-silicate (300, <100)	X
KFR02.1(240)	Mixed	15	18	0.78	±	0.085	0.046	±	0.0052			
KFR02.3(190)	Mixed	14	19	n/a	±		0.14	±	0.011			
KFM02B.2(480)	BM	9.4	15	0.17	±	0.04	0.062	±	0.0078			
KFM02B.4(410)	BM	23	16	0.8	±	0.11	0.11	±	0.013			
KFM02A.5(420)	BM	23	23	0.8	±	0.086	0.13	±	0.017			
KFM02A.3(500)	BM	148	17	0.89	±	0.1	0.061	±	0.0052	KFM02A(670)	Ca-U(VI)-silicate (<100)	X
Deposition												
KFM03A.4(630)	Trans.	34	86	9.4	±	1.4	0.1	±	0.011	KFM03A(680)	UO <sub>2+x</sub>	X
KFR105.1(150)	Glacial	32	20	1.7	±	0.17	0.24	±	0.02	KFR105(150)	UO <sub>2+x</sub>	
KFR105.5(120)	Mixed	27	16	3.9	±	0.29	0.64	±	0.046	KFR105(100)	UO <sub>2+x</sub>	
KFR02.2(210)	Glacial	12	18	n/a	±		0.71	±	0.068			
KFR02.4(150)	Mixed	17	35	n/a	±		0.21	±	0.018			
Miscellaneous												
KFR101.1(240)	Glacial	57	54	0.47	±	0.05	0.039	±	0.004			
KFR106.1(260)	Glacial	30	n/a	0.24	±	0.082	0.032	±	0.0037	KFR106(300)	Uraninite (1570)	X
KFR106.2(190)	Mixed	31	n/a	0.12	±	0.094	0.021	±	0.0026			

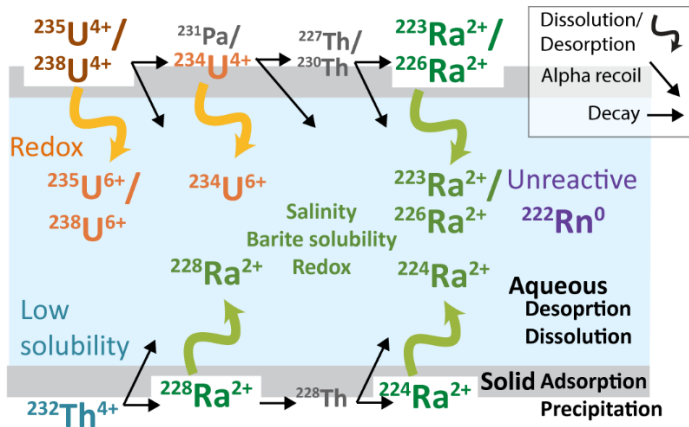


**Figure 1:** Schematic illustration showing the isotopes used in this study and the influence of geochemistry and alpha decay on their groundwater activities. Half-lives range from billions of years for  $^{238}\text{U}$  and  $^{232}\text{Th}$  to days for  $^{223}\text{Ra}$ ,  $^{224}\text{Ra}$ , and  $^{222}\text{Rn}$ . Activities for isotopes shown in grey not reported in this study.

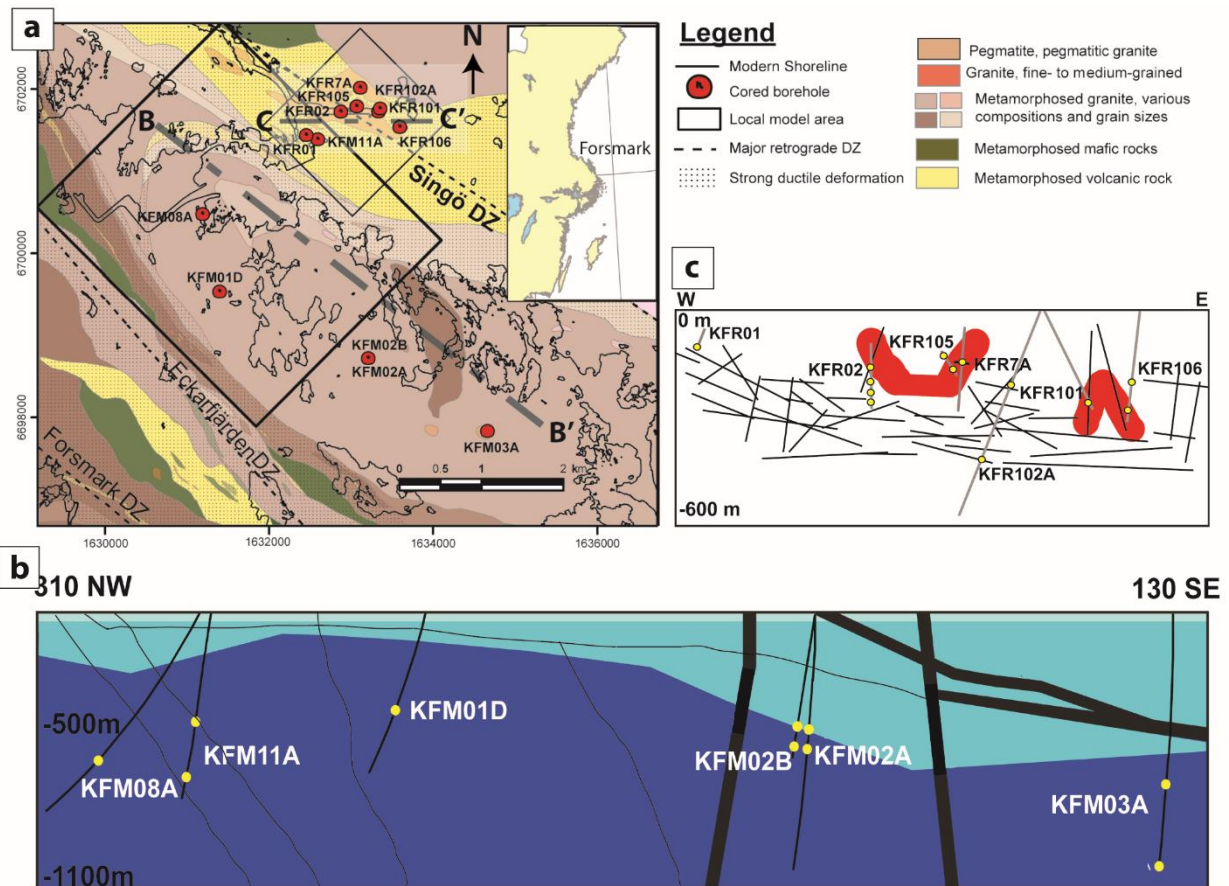


**Figure 2:** (a) Map showing relation of bedrock geology to deformation zones (name ending with 'DZ') and groundwater samples, also illustrated in cross-section for (b) Forsmark and (c) SFR sites. Some SFR boreholes are oriented sub-horizontally because they were drilled from the repository tunnel. Groundwater sampling sections

(yellow dot on borehole) shown with respect to fracture orientation and groundwater-type. Groundwater-types coded by color: light blue - meteoric recharge, medium blue – brackish marine groundwater (Littorina Sea water mixed with glacial meltwater), dark blue – mixture of pre-Holocene waters including deep saline basement water and glacial meltwater, red – pockets of dilute glacial meltwater, and white – mixed brackish marine (including modern Baltic Sea water).

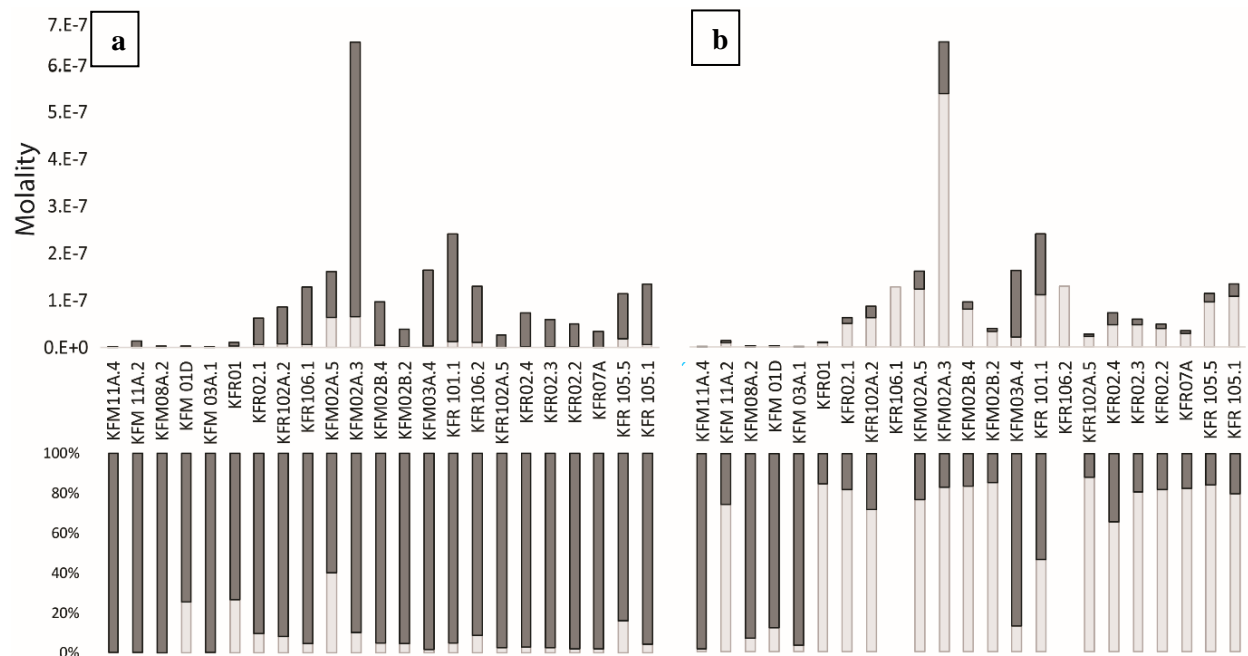


**Figure 3:** Speciation of dissolved U as U(IV)<sub>aq</sub> (dark grey) and U(VI)<sub>aq</sub> (light grey) by sample for (a) Fe(III)/Fe(II) and (b) S(-II)/S(VI) redox couples. Top Y-axis = molality. HS<sup>-</sup> concentration unavailable for KFR106.

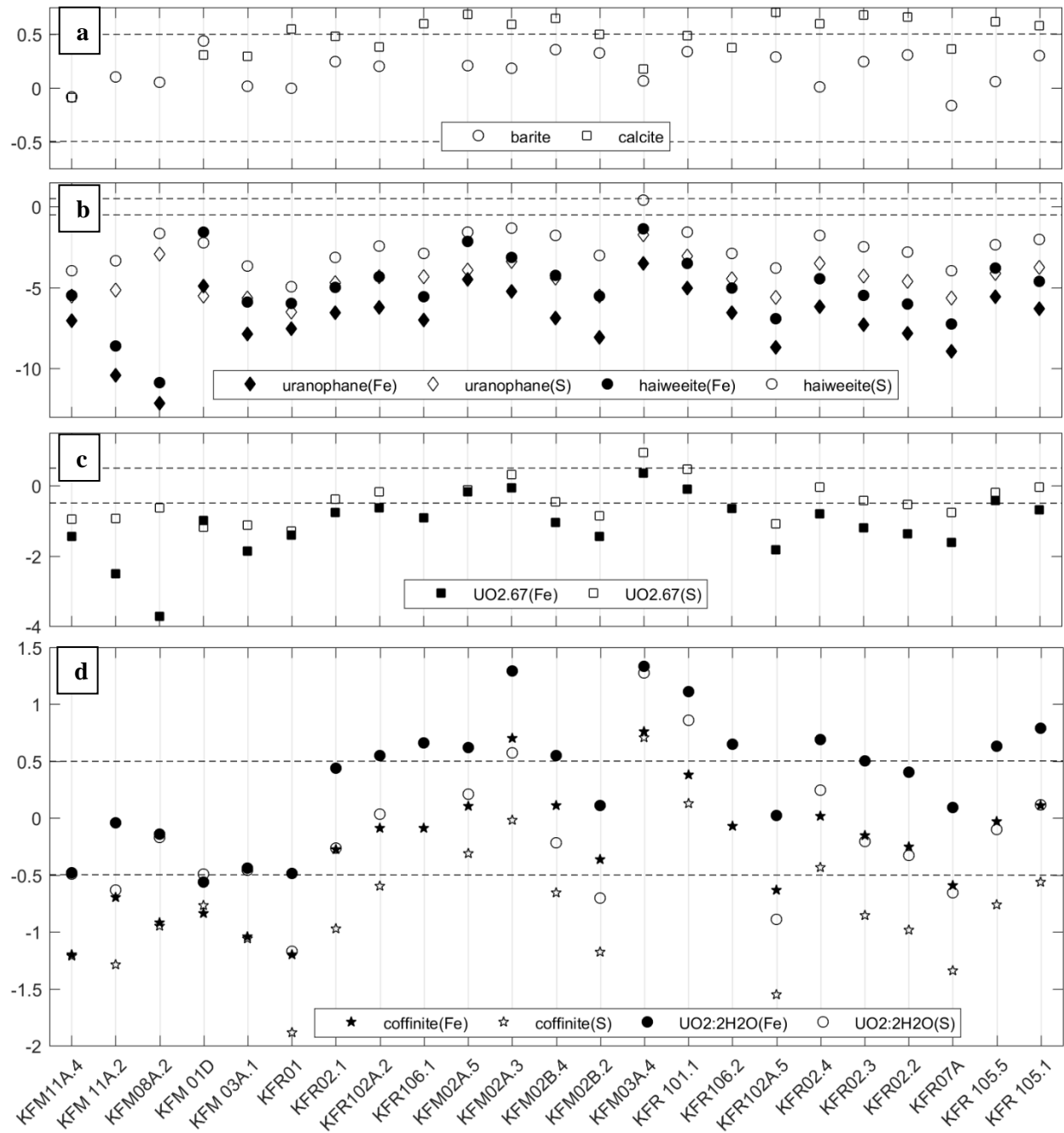


**Figure 4:** Calculated saturation indexes of phases important to the behavior of U and Ra (i.e. barite): (a) calcite and barite, (b) uranophane and haiweeite, (c)  $UO_{2.67}$ , and (d) amorphous coffinite and amorphous  $UO_2:2H_2O$ . For U phases, saturation index as calculated under Fe(II)/Fe(III) and S(-II)/S(VI) redox system are shown (filled and unfilled, respectively). Dashed lines reflect bounds of uncertainty in thermodynamic data as propagated through the saturation index calculation ( $\pm 0.5$ ), within with a solid-phase is considered to be in equilibrium.

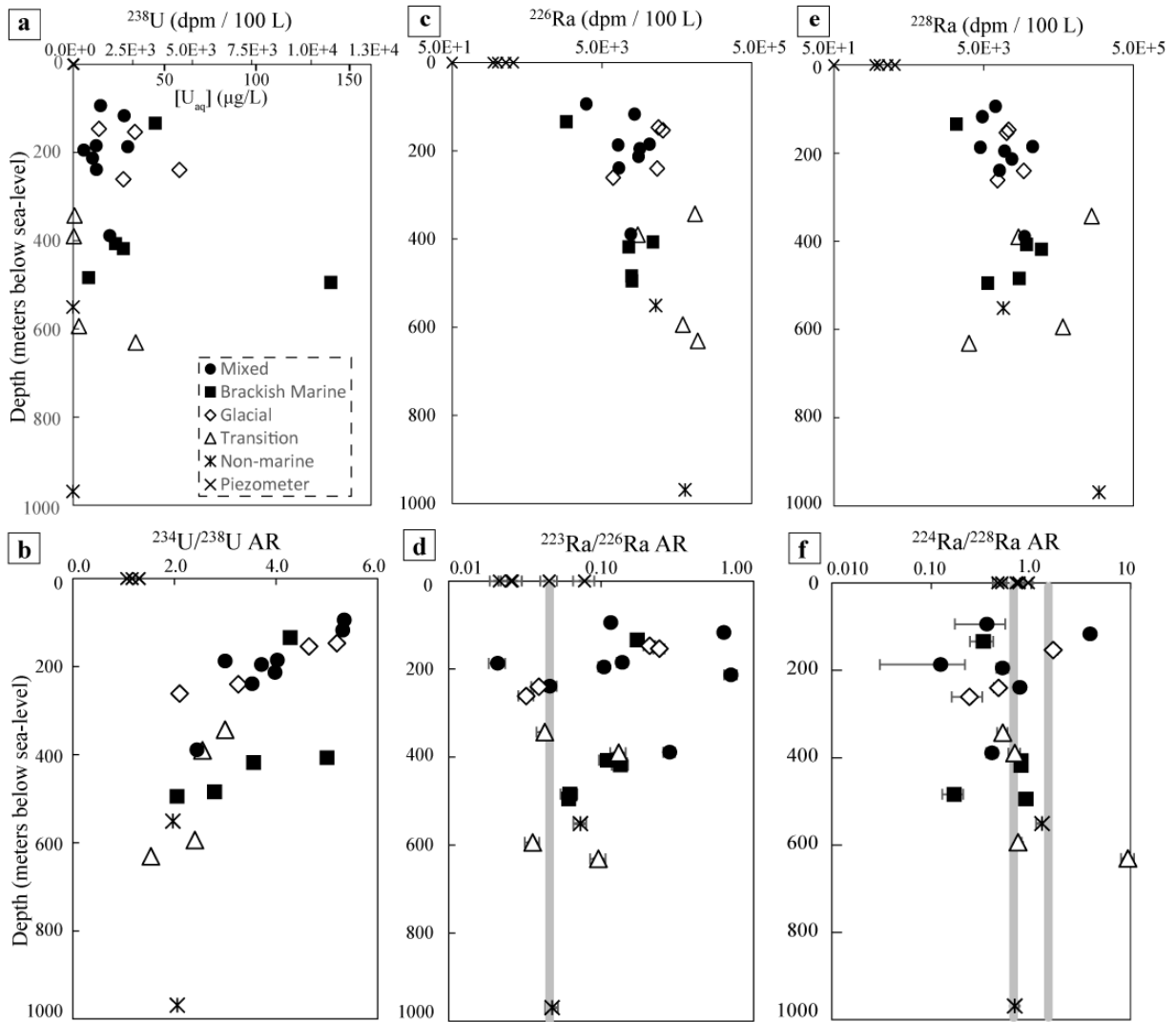


**Figure 5:** Dissolved constituents against depth (m.b.s.l.) for (a) U concentrations, (b)  $^{234}\text{U}/^{238}\text{U}$  ARs, (c)  $^{226}\text{Ra}$  activities, (d)  $^{223}\text{Ra}/^{226}\text{Ra}$  ARs, (e)  $^{228}\text{Ra}$  activities, (f)  $^{224}\text{Ra}/^{228}\text{Ra}$  activities. Bulk groundwater activities expressed in disintegrations per minute (dpm) per 100 L groundwater. Symbols larger than uncertainties of activities in a-c, e. Steady state activities noted by grey bar in d, f.

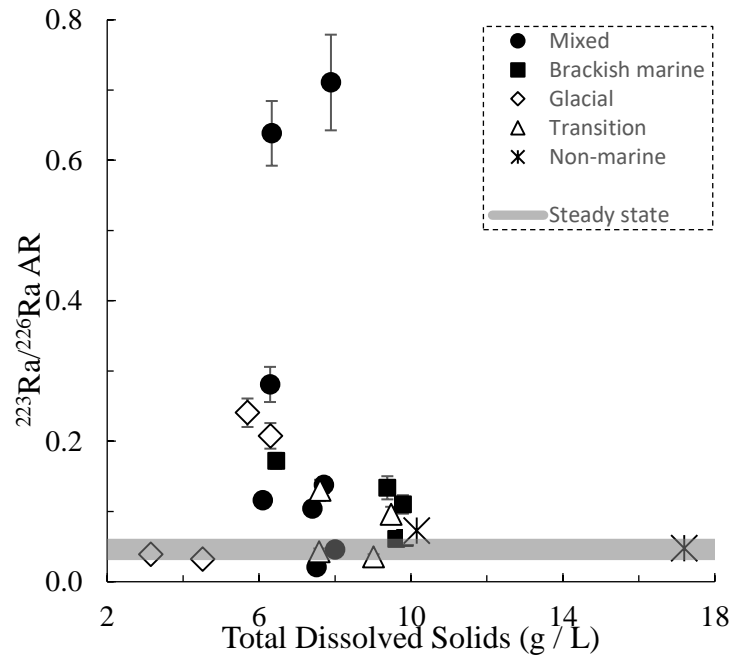


**Figure 6:**  $[^{223}\text{Ra}/^{226}\text{Ra}]_{\text{GW}}$  as a function of total dissolved solids, by groundwater type, steady state  $[^{223}\text{Ra}/^{226}\text{Ra}]_{\text{GW}}$  of 0.046 denoted by grey bar.

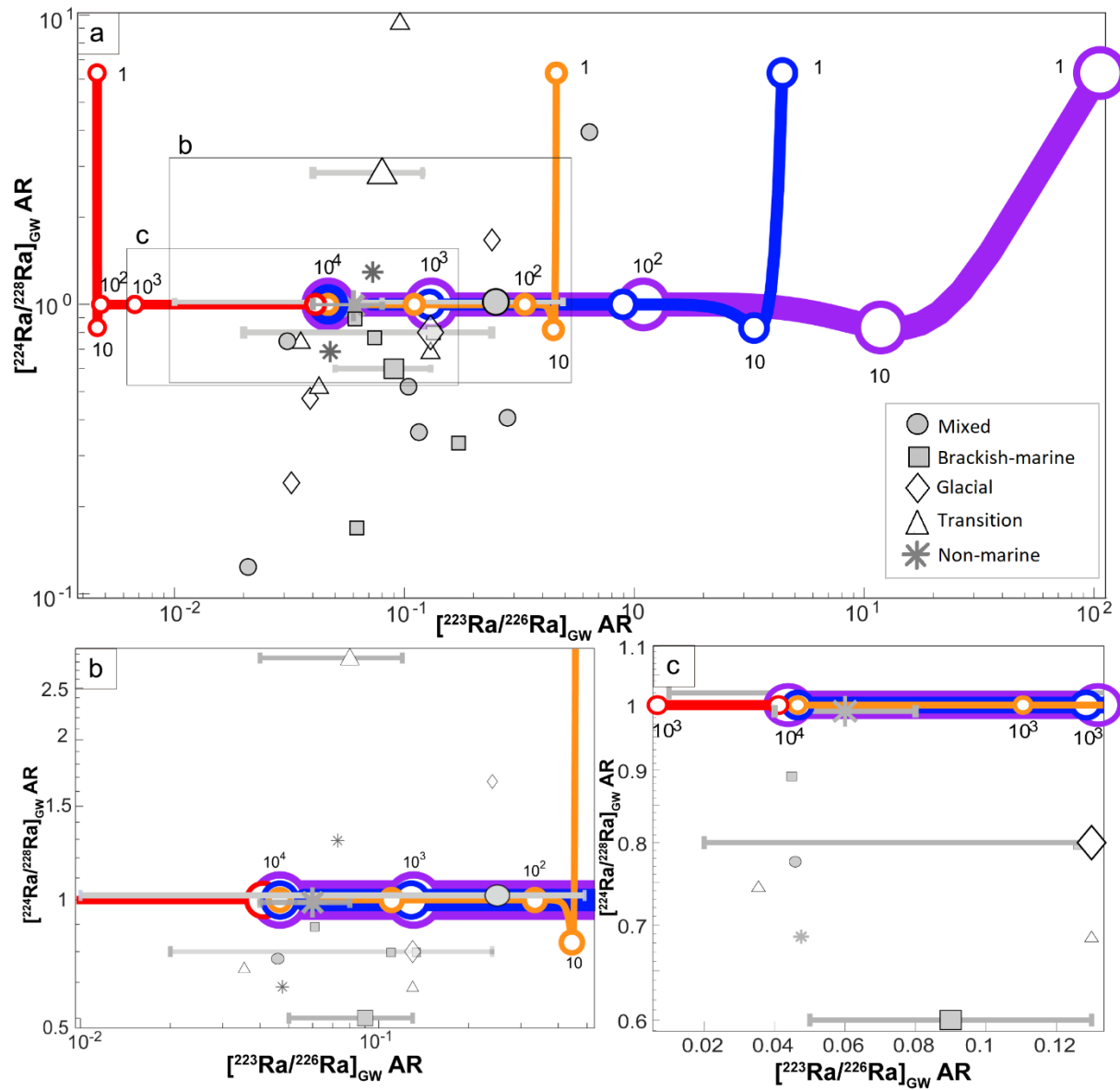


**Figure 7:** Residence time curves showing coeval  $[^{224}\text{Ra}/^{228}\text{Ra}]_{\text{GW}}$  and  $[^{223}\text{Ra}/^{226}\text{Ra}]_{\text{GW}}$  alongside  $\text{AR}_{\text{GW}}$  Forsmark/SFR results for 1 – 10,000 y (labelled next to empty circles). Mean ARs and  $1\sigma$  standard deviation for each groundwater type shown by the larger symbols. The  $[^{224}\text{Ra}/^{228}\text{Ra}]_{\text{GW}} = 1$  after ~30 y, and  $[^{223}\text{Ra}/^{226}\text{Ra}]_{\text{GW}} = 0.046$  after ~10,000 y. Red curve illustrates the low initial ARs caused by advection of long-lived  $^{226}\text{Ra}_{\text{GW}}$ , apparent in groundwater that enters a fracture environment that supports 100-times lower  $\text{Ra}_{\text{GW}}$  than the previous environment. Groundwater that enters a relatively  $\text{Ra}_{\text{GW}}$ -rich environment, wherein activities exceed that of the previous (purple) by factors of 10 (blue) and 100 (orange). Multiple curves generated simply to show that ARs can vary at time  $t_0$ , but  $[^{223}\text{Ra}/^{226}\text{Ra}]_{\text{GW}}$  converge to ~0.12 after 1000 y (7.b-7.c) as long as the new environment is relatively rich in  $U_{\text{solid}}$ .

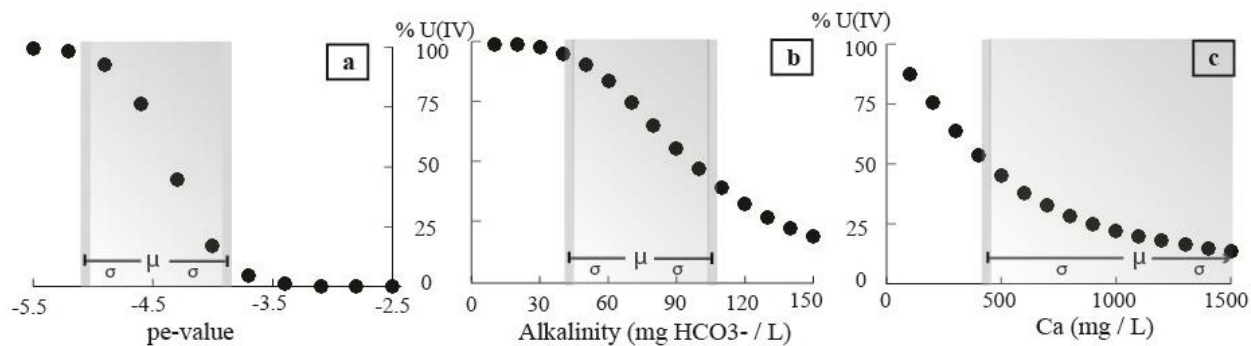


**Figure 8a-c:** Proportion of aqueous U(IV) as a function of (a) pe value, (b) alkalinity, and (c) Ca concentration in KFM02A.3, where the “μ” and grey area mark the site mean and standard deviation for the respective constituents. In (a), redox potential varied -2.5 to -5.5 while alkalinity and Ca concentrations held constant at 130 mg/L and 1000 mg/L, respectively. In (b), alkalinity varied 0 to 150 mg/L while pe and Ca held constant at -4.4 and 1000 mg/L, respectively. In (c), Ca varied 0 to 1500 mg/L while alkalinity and pe held constant at 130 mg/L and -4.4, respectively.

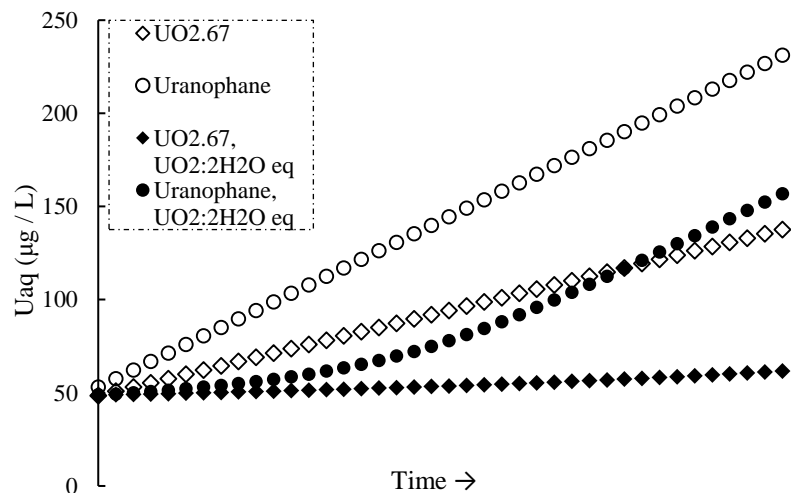


**Figure 9:** Results from forward modelling test of step-wise uranophane and UO<sub>2.67</sub> dissolution, with and without sequestration of reduced U(VI) by amorphous UO<sub>2</sub>:2H<sub>2</sub>O and coffinite. For each trial, 0.384 μm of U<sub>solid</sub> were available for the reaction. For the equilibrium trials, the amount of coffinite<sub>am</sub> + UO<sub>2</sub>:2H<sub>2</sub>O<sub>am</sub> that precipitated was 0.29 and 0.31 μmol for dissolution of uranophane and UO<sub>2.67</sub>, respectively.

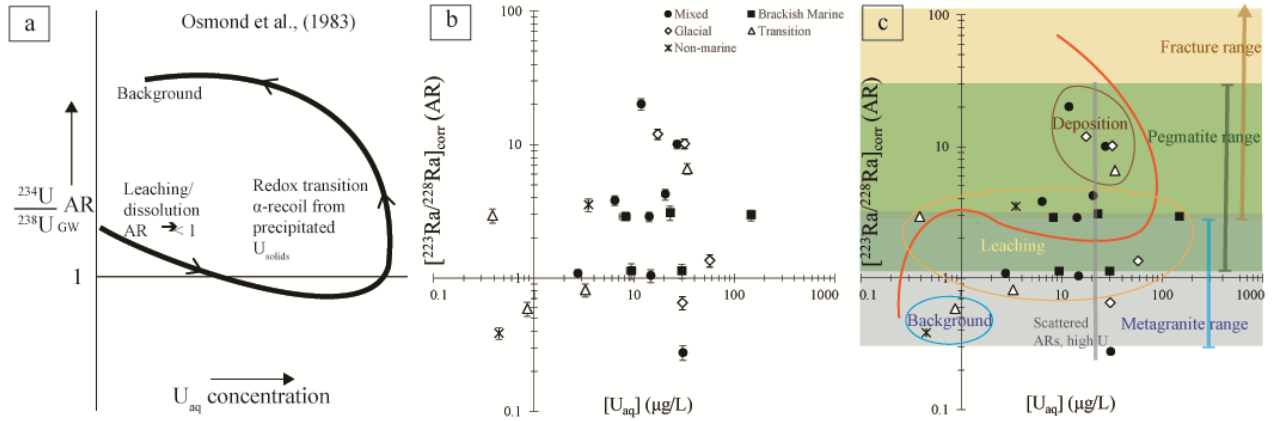
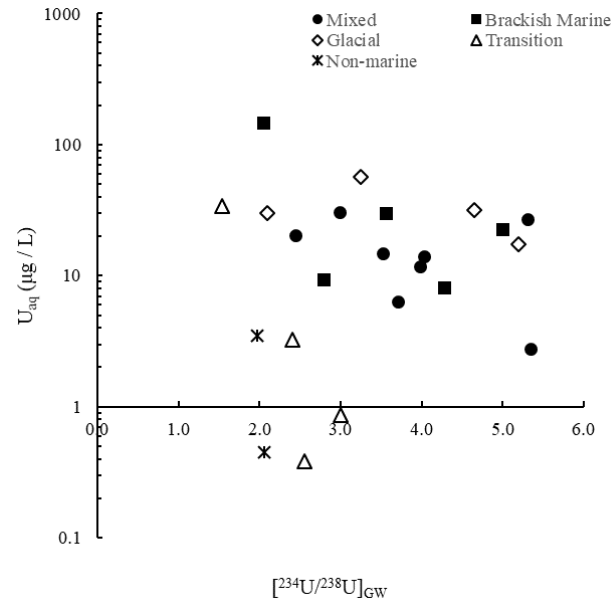


**Figure 10:** Leaching-deposition diagrams for  $[^{223}\text{Ra}/^{228}\text{Ra}]_{\text{corr}}$ , motivated by (a) Osmond et al. (1983) model for detecting redox fronts using  $[^{234}\text{U}/^{238}\text{U}]_{\text{GW}}$  and  $[\text{U}_{\text{aq}}]$ . (b) Forsmark/SFR  $[^{223}\text{Ra}/^{228}\text{Ra}]_{\text{corr}}$  plotted against  $[\text{U}_{\text{aq}}]$  and (c) interpreted curve, labelled leaching-deposition sectors, and  $[^{238}\text{U}/^{232}\text{Th}]_{\text{rk}}$  obtained from chemical analyses of various local rock types.

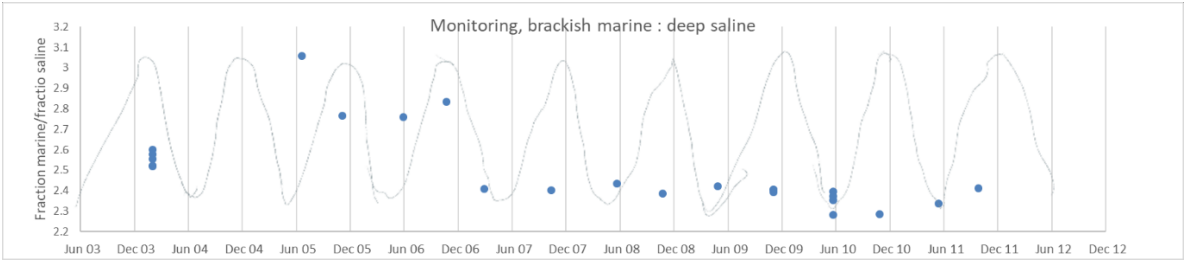
1    **Supplementary Figures**

**Figure S1:** Plot of  $[^{234}\text{U}/^{238}\text{U}]_{\text{GW}}$  versus  $U_{\text{aq}}$ , by groundwater-type.



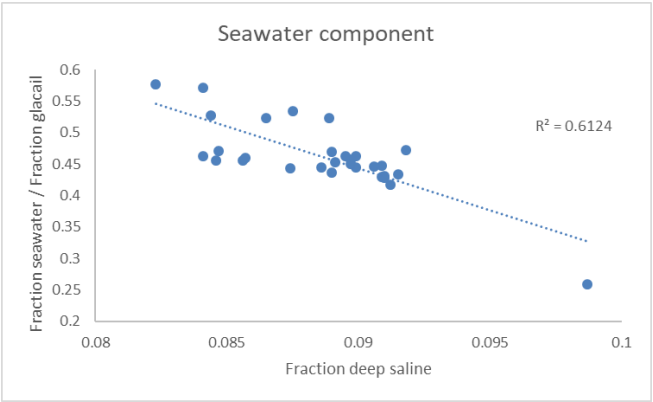
2

**a.**



**Figure S2:** Monitoring data to show the variations in the brackish-marine Littorina component in KFM03A.4(630). Fractional components calculated using system of linear equations with three unknown fractions (Littorina, glacial, and deep saline) with end-member components ( $\text{SO}_4^{2-}$ ,  $\delta^{18}\text{O}$ , and  $\text{Cl}^-$ , respectively; Laaksoharju et al., 2008). (a) Seasonal dependency of marine groundwater fraction, normalized to the deep saline fraction (b) Littorina fraction inversely proportional to glacial and deep saline fractions, implying that the Littorina (i.e. marine) component varies over time ( $\sigma \pm 10\%$ ) due to mixing at “transition” groundwater boundary.

**b.**



3